Title

Lynx1 regulates nAChRs to preserve the structure and function of neuromuscular synapses during aging

Short Title

Lynx1 role in NMJ maintenance

One Sentence Summary

Lynx1 promotes homeostatic plasticity at NMJs by regulating the function and stability of muscle-specific nAChRs.

Authors

Sydney V. Doss[1,2], Sébastien Barbat-Artigas[4], Tracey Myers[3], Bhola Shankar Pradhan[5], Tomasz J. Prószyński[5,6], Richard Robitaille[4], Gregorio Valdez[1*]

Affiliations

[1] Department of Molecular Biology, Cellular Biology, and Biochemistry, Brown University, Providence, Rhode Island, USA.

[2] Graduate Program in Translational Biology, Medicine, and Health, Virginia Tech, Blacksburg, Virginia, USA.

[3] Fralin Biomedical Research Institute, Roanoke, Virginia, USA.

[4] Département de neurosciences, Université de Montréal, Montréal, QC, Canada.

[5] Laboratory of Synaptogenesis, Nencki Institute of Experimental Biology, Polish Academy of Sciences, Warsaw, Poland.

[6] Laboratory of Synaptogenesis, Łukasiewicz Research Network − PORT Polish Center for Technology Development, Wrocław, Poland

* Corresponding Author, Email: Gregorio_Valdez@brown.edu

Abstract

Nicotinic acetylcholine receptors (nAChRs) undergo aberrant changes in diseases and with advancing age that compromise the structure and function of neuromuscular junctions (NMJs). Despite this recognition, the mechanisms that regulate muscle nAChRs remain poorly understood. Here, we ask if Lynx1, shown to regulate nAChRs in the brain, plays a similar role at NMJs. We show that Lynx1 concentrates in the postsynaptic region of NMJs where it modulates the function and stability of nAChRs in young adult mice. However, Lynx1 levels decrease at aged NMJs suggesting roles in synaptic maintenance. Supporting this possibility, deletion of Lynx1 prematurely and progressively increases the incidence of NMJs with age-related features, culminating in the atrophy of muscle fibers. These data show that by promoting homeostatic synaptic plasticity and NMJ remodeling, Lynx1 regulation of nAChRs mitigates age-related damages at NMJs.

Introduction

Molecular, structural, and functional synaptic remodeling occurs throughout development and for most of adult life in order to maintain neurotransmission within a physiological range and also as a prerequisite for connected cells to remain viable (*1*–*3*). Homeostatic synaptic plasticity is characterized by changes in neurotransmitter release from the presynapse that drive alterations in the properties and availability of receptors in the postsynapse. This is the case at the neuromuscular junction (NMJ), the synapse formed between motor neurons and muscle fibers (*1*, *4*). During development, the number and distribution of nicotinic acetylcholine receptors (nAChRs) increase at vertebrate

NMJs, allowing for postsynaptic expansion which in turn drives growth and proper apposition of the presynapse (*5*, *6*). At the same time, nAChR pentamers become less sensitive to the actions of ACh due a shift in their subunit composition (*7*). These and other changes in the post- and pre-synaptic regions culminate in maturation of NMJs that are relatively stable for most of adult life (*8*).

While nAChRs are relatively stable at healthy adult NMJs, adjustments in phosphorylation status, trafficking, clustering, and anchoring of nAChRs (*14–19*) occur in response to changes in cholinergic transmission associated with motor neuron injury and diseases. With advancing age (*9*) and the progression of diseases (*10–12*), however, the NMJ loses the capacity for homeostatic remodeling, resulting in long-term deleterious morphological and functional changes that culminate in loss of motor function. Further, there is evidence suggesting that aberrant changes in nAChRs may specifically compromise postsynaptic homeostatic plasticity (*4*) and thus contribute to degeneration of NMJs during aging (*9*) and diseases (*13*). Therefore, a better understanding of the mechanisms that regulate the function and stability of nAChRs in normal and degenerating NMJs may lead to therapies that slow or prevent age- and disease-related motor dysfunction.

Lynx1 is a small GPI-anchored protein that alters depolarization and plasticity of cholinergic synapses in the brain (*20*, *21*) through its interactions with nAChRs. Lynx1 bears structural similarity to α-bungarotoxin (*20*), which binds with high-affinity to muscle nAChRs. Unsurprisingly, Lynx1 has been shown to decrease the sensitivity of nAChRs to ACh through a direct interaction at the postsynaptic membrane in the brain (*22*). However it has also been proposed to promote the translocation of nAChR pentamers

with lower sensitivity to ACh (*23*) via preferentially binding of nAChR subunit interfaces in the endoplasmic reticulum (*24*). In the brain, Lynx1 regulation of synaptic plasticity (*25–27*) has been demonstrated to impact motor learning (*28*), nicotine addiction (*29*), nociception (*30*), neuronal survival (*31*), and pathologies caused by aging (*32*) and Alzheimer's disease (*33*). Thus, Lynx1 is a promising candidate for modulating nAChRs at NMJs during development, adulthood, and under stressed conditions such as aging and in Amyotrophic Lateral Sclerosis (ALS). However, little is known about the expression and distribution of Lynx1 in skeletal muscle or its role in postsynaptic homeostatic plasticity at the NMJ.

In the current study, we examine the expression, localization, and function of Lynx1 at mouse NMJs. We discover that Lynx1 is indeed expressed in skeletal muscles and progressively concentrates at NMJs during development. Importantly, we show that Lynx1 interacts with and modulates the activity of nAChRs at the NMJ. It also helps stabilize nAChRs at the peripheral membrane. While Lynx1 does not appear to play a meaningful role in developing NMJs, its presence helps stave off the deleterious effects of aging on NMJs and muscle fibers. Along these lines, loss of Lynx1 destabilizes the postsynapse in addition to causing presynaptic defects in adult mice, suggesting that it may affect signaling pathways important for both pre- and postsynaptic plasticity and maintenance. Altogether, this study demonstrates that Lynx1 is essential for maintaining the normal function and viability of adult NMJs and muscle fibers.

Results

Lynx1 concentrates in the postsynaptic region of the NMJ

We first sought to determine if Lynx1 is expressed specifically by skeletal muscle fibers in adult mice. To answer this question, we examined Lynx1 transcript levels in ribosome-associated mRNA fractions specifically isolated from tibialis anterior (TA) fast-type muscle fibers, which constitute the majority of fibers in this muscle. This was accomplished through mRNA-ribosome co-immunoprecipitation of hemagglutinin (HA) tagged ribosomal protein L22 (Rpl22) expressed specifically in fast-type muscle fibers in the TA under the parvalbumin promoter (*34*) in parvalbumin-Cre(*35*); RiboTag$^{flox/flox}$ (*36*) mice. This approach showed that Lynx1 is enriched in mRNA fractions isolated from fast-type muscle fiber ribosomes compared to fractions obtained from the whole TA muscle from 3-month-old (mo.) mice (Fig. 1A). Thus, Lynx1 mRNA is enriched in muscle fibers.

We then examined the expression of Lynx1 in developing skeletal muscles of wild-type mice. We found that Lynx1 transcripts increase in the TA and extensor digitorum longus (EDL) muscles as mice transition from the postnatal to the juvenile stage of life (Fig. 1B). We found a similar expression pattern for Lynx1 in maturing C2C12-derived myotubes (Fig. 1C), suggesting a close link between levels of Lynx1 and the induction of nAChR expression (*37*) as well as other molecular and functional changes associated with maturation of muscle fibers and NMJs. To further assess the relationship between Lynx1 and the NMJ, we generated an antibody to immunostain skeletal muscles for Lynx1. This analysis showed that Lynx1 protein localizes specifically at NMJs where it gradually increases during development (Fig. 1D-F). These complementary experiments

demonstrate that muscle fibers express and concentrate Lynx1 in the postsynaptic region of the NMJ.

Lynx1 interacts with nAChRs of the NMJ

Lynx1 has been demonstrated to closely associate with neuronal isoforms of nAChR subunits (*20–24*, *31*), acetylcholine binding protein (AChBP) from *L. stagnalis*, and muscle nAChRs in *torpedo californica* (*22*). However, it remains unknown if Lynx1 interacts with mammalian NMJ-specific nAChR subunits. We performed a series of biochemical experiments to analyze the interaction of Lynx1 with an nAChR pentamer consisting of the four subunits unique to mammalian adult NMJs (α1, β1, δ, and ε). We co-transfected HEK293 cells with all four nAChR subunits along with mCherry-tagged Lynx1 (mCherry-Lynx1) (*23*). Demonstrating successful co-transfection, both nAChR pentamers and mCherry-Lynx1 were readily detected in cell lysates from HEK293 cells with Western blot using antibodies against the nAChR pentamer and mCherry (Fig. 2A, lane 1). Specificity of the nAChR antibody was confirmed by Western blot of HEK293 cell lysate collected following transfection of Lynx1-mCherry but not the nAChR subunits (Fig. 2A, lane 2). We then performed co-immunoprecipitation (co-IP) assays of transfected HEK293 cell lysates using an antibody against the nAChR and probed Western blots for both nAChR and mCherry. We found that mCherry-Lynx1 co-immunoprecipitated only from HEK293 cells co-expressing nAChR pentamers (Fig. 2A, lanes 3-5). This finding suggests that Lynx1 interacts with the muscle-specific nAChR pentamer located at mammalian NMJs.

Lynx1 is thought to directly interact with the extracellular domain of neuronal nAChRs (*22*). To determine whether a similar interaction occurs with muscle-specific nAChR subunits, we asked whether glutathione S-transferase (GST)-tagged ectodomains of the α1, β1, δ, ε, and γ nAChR subunits, were capable of pulling down mCherry-Lynx1 from HEK293 cell lysates. Western blotting for both mCherry and GST showed that the ectodomains of all muscle-specific nAChR subunits are capable of pulling down mCherry-Lynx1 (Fig. 2B). Thus, Lynx1 interacts with the extracellular domain of each NMJ-specific nAChR subunit. This promiscuous association of Lynx1 with multiple nAChR subunits has been shown previously in the CNS (*29*).

We next assessed the possibility that the pull-down of Lynx1 by nAChR ectodomains may have occurred through indirect interactions with extraneous proteins within the HEK293 cell lysate. To do this, we tested the ability of alpha-bungarotoxin (BTX), which binds the α1 nAChR subunit with high affinity (*38*), to pull down Lynx1 from a solution of purified recombinant GST-tagged Lynx1 and α1 nAChR ectodomain proteins. Providing evidence for a direct interaction between Lynx1 and an NMJ-specific nAChR pentamer, we found that BTX pulls down both the α1 nAChR subunit and Lynx1, as revealed by Western blot using an anti-GST antibody (Fig. 2C). To further establish that Lynx1 directly interacts with the ectodomains of NMJ-specific nAChR subunits, we asked whether each of the GST-tagged nAChR ectodomains (α1, β1, δ, ε, and γ) are capable of pulling down 6x histidine-tagged water soluble Lynx1 (*39*) (Lynx1-6x-His) from purified protein solutions. Again, Lynx1-6x-His was successfully pulled-down by each of the muscle-specific nAChR ectodomains (Fig. 2D). Collectively, these experiments

strongly indicate that Lynx1 directly interacts with each of the 5 muscle-specific nAChR subunits found in mammalian NMJs.

Lynx1 modulates the sensitivity of nAChR to ACh in skeletal muscles

We sought to determine if Lynx1 also modulates the function of nAChRs at the NMJ. We examined miniature endplate potentials (MEPPs), a direct readout of the biophysical properties of postsynaptic nAChRs, in NMJs of 4 mo. Lynx1$^{-/-}$ and control mice. This analysis showed that the rise time, which reflects the binding of ACh to nAChRs, was significantly faster in NMJs of Lynx1$^{-/-}$ compared to control mice (Control = 1.33 ±0.0952 ms; Lynx1$^{-/-}$ = 0.857 ±0.1321 ms, p = 1.66E-27; Fig. 3A-C). Supporting this finding, the slope to reach the maximum MEPP amplitude was steeper at NMJs lacking Lynx1 (Fig. 3D). Despite these differences, deletion of Lynx1 did not affect the mean amplitude (Fig. 3E) or frequency (Fig. 3F) of MEPPs. Further, loss of Lynx1 did not alter the EPP amplitude (Fig. 4A-B), or the quantal content (Fig. 4C) at NMJs. These data indicate that while the binding of ACh to nAChRs and the postsynaptic response was facilitated, the probability of presynaptic ACh release remained unaltered at NMJs in Lynx1$^{-/-}$ mice.

Given that Lynx1 decreases cholinergic sensitivity at the NMJ, we next examined if Lynx1 modulates postsynaptic desensitization to sustained cholinergic signaling. To do so, we observed changes in EPP amplitude in control and Lynx1$^{-/-}$ muscle following sustained motor nerve stimulation (120 hz at 10s intervals). At NMJs of control mice, we observed a characteristic early rapid depression (74.96±1.589%; Fig. 4D, orange arrow) that was followed by a delayed, long-lasting depression (11.88±3.635%; Fig. 4D, blue arrow). In NMJs of Lynx1$^{-/-}$ mice, a characteristic rapid synaptic depression following initial

stimulation was produced (77.74±1.553%; Fig. 4D, orange arrow), however, this was followed by a significant post-tetanic potentiation event (12.22±3.688%) (Fig. 4D, green arrow), and an obliteration of EPP depression throughout sustained stimulation (Fig. 4D, blue arrow). Taken together, these data indicate that Lynx1 dampening of nAChR sensitivity is utilized for rapid desensitization of skeletal muscles during periods of heightened cholinergic activity.

Lynx1 stabilizes nAChRs at the peripheral membrane

The stability of nAChRs on the post-synaptic membrane of the NMJ has been shown to be tightly linked to cholinergic transmission. Given that Lynx1 regulates cholinergic signaling and directly interacts with muscle-specific nAChR subunits, we asked if Lynx1 plays a secondary role in stabilizing nAChRs at the NMJ. To test this possibility, we labeled nAChRs with saturating amounts of Alexa Fluor-488 conjugated BTX (A488-BTX) in the sternomastoid muscle of anesthetized 3 mo. Lynx1$^{-/-}$ and control mice. BTX irreversibly binds nAChRs with high affinity (*38*), allowing for extended *in vivo* labeling of nAChRs. After 48 hours, mice were sacrificed and the sternomastoid muscles were stained with Alexa Fluor-555 conjugated BTX (A555-BTX) to label nAChRs that were inserted during the 48h period following initial exposure to A488-BTX (*40*) (Fig. 5A-C). Demonstrating the validity of this approach, A555-BTX failed to label NMJs in the sternomastoid muscle when it was fixed immediately following exposure to saturating concentrations of A488-BTX (Supplementary Figure 1). To determine the amount of nAChR turnover, we measured the fluorescence intensity of newly inserted A555-BTX labeled nAChRs as a percentage of the combined fluorescence intensity of both A555-BTX and A488-BTX labeled nAChRs at each NMJ (Fig. 5D-E). In NMJs of the

sternomastoid of Lynx1$^{-/-}$ mice, the average percentage of new nAChRs was significantly higher compared to control mice (Fig. 5F), suggesting an increased rate of nAChR turnover during the 48 h period of analysis. These data show that Lynx1 stabilizes nAChRs at NMJs in addition to modulating their sensitivity to ACh.

Lynx1 is reduced at aged NMJs

The stability and density of nAChRs decrease with advancing age (*18*, *41–44*). These changes are accompanied by impaired cholinergic transmission and deficits in NMJ remodeling leading to loss of pre- and post-synaptic apposition (*9*). We thus asked if Lynx1 undergoes aberrant changes that could potentially contribute to aging of NMJs. To start, we compared Lynx1 distribution and expression between old and young NMJs. Immunostaining and light microscopy analysis showed that Lynx1 is markedly reduced in NMJs of 24 mo. compared to 4 mo. mice (Fig. 6A-C). The loss of Lynx1 from aged NMJs does not result from decreased mRNA expression since Lynx1 transcripts were at similar levels in the TA muscle of old and young mice (Fig. 6D). The decreased concentration of Lynx1 at aged NMJs occurred despite increased expression of most nAChR subunits (Fig. 6E). Thus, deficits in Lynx1 at aging NMJs may enhance nAChR instability and aberrant post-synaptic remodeling associated with dysregulated cholinergic transmission that contribute to neuromuscular degeneration (*44*).

Lynx1 loss accelerates aging of NMJs

The impact of Lynx1 on nAChR function and stability (Fig. 3, Fig. 4) suggests that Lynx1 may be important for NMJ development and maintenance. To answer this question, we first determined whether NMJs develop normally in the absence of Lynx1. We examined NMJs in the EDL muscle of postnatal day 6 (P6), P9, and P21 control and

Lynx1$^{-/-}$ mice, ages in which NMJs and muscle fibers undergo fast and dramatic morphological, molecular, and functional changes (*8*). At each of these ages, NMJs were morphologically indistinguishable between control and Lynx1$^{-/-}$ mice (Supplementary Figure 2A-J). Furthermore, deletion of Lynx1 did not affect expression of genes critical for the formation and maturation of NMJs, including nAChR subunits and muscle-specific kinase (MuSK) (Supplementary Figure 2K-L). Taken together, these data show that NMJs develop normally in the absence of Lynx1, achieving a mature pretzel-like structure at 21 days of age.

We next examined the morphology of NMJs in the EDL muscle of 4 mo. mice lacking Lynx1.This analysis revealed that NMJ integrity is compromised in Lynx1$^{-/-}$ compared to control mice (Fig. 7A-B). We observed changes in several morphological characteristics associated with poor NMJ health, including loss of innervation by motor axons (Fig. 7C), increased fragmentation of nAChR clusters of the post-synapse (Fig. 7C), decreased nAChR intensity (Fig. 7E), corroborating our findings of increased nAChR turnover, and increased blebbing of the motor axon terminal (Fig. 7F). Other morphological indices of NMJ integrity were unchanged in Lynx1$^{-/-}$ muscle, including post-synaptic area (Fig. 7D) and innervation by more than one motor axon (Fig. 7F).

To determine if NMJs lacking Lynx1 accrue age-related deleterious cellular and molecular features at a faster rate than controls, we extended our analysis to 12 mo. mice (Fig. 8A-B). We again found a higher incidence of denervated and fragmented NMJs in middle-aged Lynx1$^{-/-}$ mice compared to age- and sex-matched control mice (Fig. 8C). Middle-aged Lynx1$^{-/-}$ mice also presented with smaller receptor area (Fig. 8D) and reduced nAChR density, revealed by the lower intensity of fluorescently labeled BTX

(fBTX, Fig. 8E). Additionally, middle-aged Lynx1$^{-/-}$ mice had more multiply innervated NMJs and innervating motor axons with large blebs, a hallmark of degenerating axons (Fig. 8F).

To complement these cellular data, we examined the expression of genes that are critical for the stability and function of the NMJ and are known to be differentially regulated by skeletal muscles with increasing age, including the α1, β1, δ, and ε nAChR subunits, acetylcholinesterase (AChE), LDL Receptor Related Protein 4 (LRP4), and MuSK. As expected, these genes, with the exception of Rapsyn, were upregulated at 12 months of age in the TA of control mice. Interestingly, this same group of genes was upregulated in the TA of young adult Lynx1$^{-/-}$ muscle, as compared to controls (Fig. 8G-H). Further, we observed a less robust age-related increase in a number of these genes, including the α1, β1, δ, ε, and γ nAChR subunits, in 12 mo. Lynx1$^{-/-}$ versus control muscle (Fig. 8G). Given the extent of NMJ deterioration in Lynx1$^{-/-}$ muscle at this age (Fig. 8A-F), the weak upregulation of these key NMJ associated molecules is suggestive of an impaired homeostatic response. Together, these results provide evidence that loss of Lynx1 accelerates the appearance of age-related features at NMJs.

Muscle atrophy follows deleterious changes at NMJs in mice lacking Lynx1

It is plausible that deletion of Lynx1 indirectly impacts NMJ integrity via deleterious extra-synaptic changes in muscle fibers. To address this possibility, we examined adult Lynx1$^{-/-}$ muscle fibers for signs of atrophy, including reduced muscle fiber size and increased presence of muscle fibers undergoing cycles of degeneration and regeneration (Fig. 9A-D). Specifically, we measured the cross-sectional area of the whole TA muscle and the muscle fiber area (MFA) of individual muscle fibers, and we determined the

incidence of regenerating muscle fibers based on the presence of myonuclei near the center of the sarcoplasm (*45*). This analysis revealed no signs of muscle atrophy in Lynx1$^{-/-}$ muscle at 4 months of age. The cross-sectional area (CSA) of the whole TA (Fig. 9E), the average MFA of individual muscle fibers (Fig. 9F), the distribution of MFAs (Fig. 9G), and number of muscle fibers exhibiting signs of regeneration were similar between mice with and without Lynx1 at 4 months of age (Fig. 9H). Thus, despite the clear signs of NMJ degeneration (Fig. 7), muscle fibers appear normal in Lynx1$^{-/-}$ muscle at 4 months of age. This provides strong evidence that NMJ deterioration is a direct consequence of Lynx1 deletion, rather than a secondary effect related to muscle fiber atrophy. By 12 months of age, there was clear evidence of muscle atrophy in Lynx1$^{-/-}$ mice. The average TA CSA and MFA were reduced in Lynx1$^{-/-}$ compared to control mice (Fig. 9E-F). Along with these changes, the loss of Lynx1 increased the number of muscle fibers with a small MFA (Fig. 9G) and muscle fibers exhibiting features of degeneration and regeneration (Fig. 9H).

To determine whether deletion of Lynx1 alters functional properties of skeletal muscles at 4 months of age, despite the absence of histopathological evidence of muscle atrophy, we assessed muscle contractile force independently of the NMJ. We measured the contractile properties of the EDL muscle using a force transducer following direct stimulation. We found that muscles lacking Lynx1 generated significantly less force as compared to controls (Control=59.16±2.243%; Lynx1$^{-/-}$=47.15±3.831%, p=0.0186 at 1min; Fig. 9I). These data provide some evidence of declining health and function of skeletal muscles in Lynx1$^{-/-}$ mice at 4 months of age that precede obvious morphological changes.

We also examined expression of several genes associated with myogenesis and muscle health in the TA muscle of 4 and 12 mo. Lynx1$^{-/-}$ and control mice. Of note, we found mRNA levels of Pax7, a transcriptional regulator of myogenic satellite cells[37,38], to be reduced in 4 and 12 mo. Lynx1$^{-/-}$ mice compared to age- and sex-matched control mice (Fig. 9J). In addition, deletion of Lynx1 altered the expression of several regulators of proteostasis and metabolism, including mammalian target of rapamycin (mTOR), peroxisome proliferator-activated receptor gamma coactivator 1-alpha (PGC1α), and peroxisome proliferator-activated receptor γ (PPARγ), (Sup. Fig. 3). Taken together, these data provide evidence that Lynx1 plays important roles in slowing pathological features that accrue at NMJs and eventually elsewhere in skeletal muscles with advancing age.

Discussion

The data in this study support important roles for Lynx1 in maintaining the normal function and structure of adult NMJs by modulating the activity and stability of nAChRs. As in the CNS (*20*, *22–27*), we show that Lynx1 binds nAChRs, alters their sensitivity to ACh and anchors them in the postsynaptic region of the NMJ. We then provide compelling evidence indicating that these functions of Lynx1 are important for staving off the deleterious effects of aging on NMJs. We show that Lynx1 is significantly reduced at NMJs of 24 mo. mice and its deletion accelerates the appearance of age-related features at NMJs of young adult and middle-aged mice. While muscle fibers appear morphologically normal in young adult Lynx1$^{-/-}$ mice, they display significant atrophy in these mice by 12 months of age. The timing of these events suggests that muscle atrophy is secondary to NMJ degeneration and not vice versa. These results are also in line with

our previous work demonstrating that changes in NMJ health can occur independently of muscle fiber health and possibly influence it (*46*).

This study is the first to examine Lynx1 interactions with muscle-specific nAChRs. Previous studies have uncovered two mechanisms by which Lynx1 interacts with CNS-specific nAChRs, including at the interface of α4/α4 nAChR subunits in the endoplasmic reticulum (*23*) and at the extracellular domain of nAChR pentamers at the cell surface (*22*). In a series of pull-down assays we show that Lynx1 interacts with muscle-specific nAChR pentamers in HEK293 cells co-transfected with Lynx1 and the α1, β1, δ, and ε nAChR subunits. We also show that Lynx1 is capable of interacting specifically with the extracellular domains of each muscle specific nAChR subunit (α1, β1, δ, ε, and γ). Interestingly, we were able to efficiently pull down α1 nAChR-Lynx1 complexes from HEK293 cell lysate with purified BTX. In contrast to neuronal nAChR subunits (*22*), these results suggest that while Lynx1 interacts with the nAChR extracellular domain, competition with BTX for binding is limited. These interactions appear to modulate nAChR function, as demonstrated by our electrophysiological results, in addition providing stability, as demonstrated by increased turnover of nAChRs at the NMJ in adult muscle lacking Lynx1. To our knowledge, this is the first evidence of the ability of Lynx1 to influence nAChR stability and it may be a novel mechanism through which Lynx1 influences homeostatic synaptic plasticity.

In the developing CNS, Lynx1 upregulation drives the closure of enhanced synaptic plasticity of cholinergic circuits (*26*, *47*). Suggesting a similar role at NMJs, we observed a significant increase in postsynaptic accumulation of Lynx1 at the conclusion of NMJ development, peaking at P21 (Fig.1F). However, we found no morphological

differences between NMJs of Lynx1$^{-/-}$ and control mice at P6, P9, or P21 suggesting a limited role, if any, for Lynx1 in regulating structural plasticity at developing NMJs. The possibility that Lynx1 deletion impacts nAChR function without affecting NMJ morphology during development, however, was not explored in this study.

Our electrophysiological results showing faster MEPP rise time and an absence of EPP depression following sustained motor nerve stimulation demonstrate that adult skeletal muscles lacking Lynx1 are more sensitive to cholinergic signaling. This dampening of nAChR sensitivity by Lynx1 has been observed in the CNS and is thought to be a primary mechanism by which Lynx1 modulates synaptic plasticity (*20*, *21*). The ability of Lynx1 to dampen cholinergic sensitivity at the NMJ suggests that it may have a similar role in modulating plasticity in adult skeletal muscles. The NMJ remains relatively stable throughout adulthood and experiences intermittent homeostatic plasticity events associated with exercise, nerve injury, and progressive neurodegeneration. These events are characterized by axonal sprouting, multiple innervation, and alterations in nAChR subunit expression that influence ACh sensitivity (*9*, *13*, *48–50*). While temporary windows of plasticity are important for NMJ health, it is equally important that they are closed in a timely fashion to restore normal function. Therefore, it is possible that, similar to the CNS, skeletal muscles utilize Lynx1 to modulate nAChR sensitivity in order to preserve synaptic health by controlling the timing of homeostatic plasticity.

Age-associated declines in Lynx1 may augment the deleterious effects of dysregulated cholinergic transmission on NMJ health (*51*). Evidence of dysregulated cholinergic transmission in aged NMJs includes increased amplitude and/or frequency of MEPPs, EPPs (*52–55*), and spontaneous giant miniature endplate potentials (GMEPPs),

which occur when ACh is released from vesicles residing outside the active zone(*9*), as well as altered biophysical properties of NMJs (*56*). Given that Lynx1 desensitizes nAChRs to ACh (Fig. 3), its loss from aged NMJs may amplify damages associated with dysregulated cholinergic transmission. Further, it may be a contributing factor to nAChR instability, which has been well characterized in aging NMJs (*18*, *41–44*). Studies in the CNS add further support to the protective potential of Lynx1 at aged NMJs, where deletion of Lynx1 leads to age-associated increases in neuronal degeneration in the striatum (*32*) and decreased Lynx1 levels are associated with elevated pathology in a mouse model of AD (*33*).

While this study unraveled a number of key roles of Lynx1 at NMJs and in skeletal muscles, it also raised a number of additional questions. Of particular interest is the identity of molecular mechanisms that regulate Lynx1 expression in skeletal muscles during development and throughout aging. Given that increases in Lynx1 expression are coincidental with increases in cholinergic activity in the developing NMJ, it is plausible that cholinergic signaling mediates Lynx1 expression in skeletal muscles. However, signaling pathways associated with muscle fiber maturation (*57*) and NMJ stabilization, including those downstream of z-agrin (*58*), as well as post-translational modifications of Lynx1 by GPI-cleaving enzymes (*59*) cannot be ruled out. A better understanding of how pathways located both up- and downstream of Lynx1 are affected by synaptic changes will provide a broader understanding of the role of Lynx1 in coordinating homeostatic synaptic plasticity at the NMJ. A second outstanding question concerns the mechanism by which Lynx1 stabilizes nAChRs at NMJs. Possibilities include linkages with cytoskeletal proteins or alterations in phosphorylation status due to decreased binding to

ACh. Finally, a precise mechanistic link between postsynaptic Lynx1 and presynaptic integrity remains to be determined. Given that motor neuron health and presynaptic structure are influenced by postsynaptic remodeling (*5*) and muscle-derived molecules such as FGFBP1 (*60*), Dach2, and HDAC9 (*61*), it is possible that muscle-derived Lynx1 could impact presynaptic integrity through its influence on nAChR stability and post-synaptic structure. A better understanding of these unanswered questions about Lynx1 could shed light on opportunities to promote homeostatic synaptic plasticity in order to mitigate the ravages of aging and other conditions, including ALS, nerve injuries and myasthenia gravis, on NMJs and muscles fibers (*44*, *48*, *62*).

Materials and Methods

Animals

Lynx1$^{-/-}$ mice (*31*) were obtained from the lab of Dr. Morishita and mated with Thy1-YFP16 (*63*) (RRID:IMSR_JAX:003709) animals to generate Lynx1$^{+/-}$;Thy1-YFP animals. In order to have littermate pairs, Lynx1$^{+/-}$;Thy1-YFP mice were mated together to yield litters with Lynx1$^{-/-}$;Thy1-YFP and Thy1-YFP control mice. The colony was maintained on a C57BL/6 background. Parvalbumin-Cre (*35*) (RRID:IMSR_JAX:017320), and RiboTag (*36*) (RRID:IMSR_JAX:011029) mice were obtained from Jackson Laboratories (Bar Harbor, ME) and bred to generate PVCre; RiboTag$^{flox/flox}$ offspring. Mice were sacrificed with a lethal dose of isoflurane and muscles were immediately dissected for collection of fresh frozen tissues, or transcardial perfusion with 1XPBS (pH 7.4) followed by 4% paraformaldehyde (PFA, pH 7.4) was performed to fix tissues. Male mice were used exclusively in this study. All experiments were carried out under the NIH and Canadian Council of Animal Care guidelines and animal protocols approved by the Virginia Tech

Institutional Animal Care and Use Committee (IACUC #18-148 & 18-176), the Brown University Institutional Animal Care and Use Committee (IACUC #19-05-0013), and the Comité de déontologie animale of Université de Montréal.

C2C12 cultures

C2C12 cells were plated in 8-well Flexiperm chambers on Permanox slides (ThermoFisher, 160005) coated with Poly-L-Ornithine (3 µg/mL; Sigma-Aldrich; P2533) and laminin (10 µg/mL; Thermo Fisher Scientific; 23017015) in Dulbecco's Modified Eagle Medium (DMEM, Life Technologies). Myoblasts were plated at 100,000 cells per well in culture media (high-glucose DMEM, 20% fetal bovine serum, 1× Glutamine, pen-strep, Fungizone) and incubated at 37°C and 5.0% CO_2. Twenty-four hours post-plating, the media was replaced with fusion media (high-glucose DMEM, 2% horse serum, 1× Glutamine, Pen strep, Fungizone). Myoblasts were then incubated for 3 to 7 days following the addition of fusion media to generate myotubes. RNA was extracted from myotubes at 0, 3, and 7 days post-fusion using an Aurum Total RNA mini kit (Bio-Rad), following manufacturer's instructions.

Affinity pull-down assays

Plasmid Constructs: The coding sequences of the nAChR subunit ectodomains, with the signal sequences removed, were cloned into a pGEX-4T1 vector. This included the following amino acid (aa) portions for each subunit: α1, aa21-230; β1, aa 26-238; δ, aa 25-248; ε, aa 21-239; and γ, aa 23-240. The coding sequence of Lynx1 (amino acids 21-92) with the signal sequence and the GPI anchoring signal removed (*39*) was cloned either into pGEX-4T1 vector (for GST tag) or pET-28a (+) vector for 6-His tag. The plasmids encoding the full-length α, β, δ, and ε nAChR subunits were a kind gift from Dr.

Lin Mei. The plasmid pLynx1-mCherry, as described in Nichols et al (*23*), was obtained from Dr. Henry A. Lester through Addgene.

Recombinant protein purification: The GST-tagged nAChR subunit ectodomains and Lynx1 (GST or 6-His tagged) were purified as previously described(*64*). BL21 E. coli were transformed with the respective constructs, grown in 200 ml cultures at 18°C until achieving A600 between 0.4 and 0.6. Protein expression was induced by 0.5 mM isopropyl 1-thio-β-d-galactopyranoside (IPTG) for 4 h at 18 °C. Bacteria were collected, incubated for 30 min at 4 °C in lysis buffer (50 mM NaH2PO4, 300 mM NaCl, 10 µg/ml leupeptin, 10 µg/ml aprotinin, 1 µl/ml Triton X-100, 10 µg/ml DNase I, and 15 units/µl Lysozyme), lysed by sonication for 1 min, and centrifuged at 13.8 x g for 30 min. The supernatants containing the GST-fusion proteins were incubated overnight with 20 µl of equilibrated glutathione beads (GE Healthcare #17-0756-01). The beads were washed three times with washing buffer (4.3 mM Na2HPO4, 1.47 mM KH2PO4, 137 mM NaCl, and 2.7 mM KCl) and the proteins were eluted with elution buffer (10 mM glutathione 50 mM Tris pH = 8.0). Similarly, the beads containing 6-His-tagged Lynx1 were washed three times with His wash buffer (50 mM Tris-Cl pH 8.0, 100 mM NaCl, 20 mM Imidazole). The proteins were eluted with elution buffer (10 mM glutathione, 50 mM Tris, pH 8.0 for GST tagged protein and 200 mM imidazole in 50 mM NaCl, 50 mM Tris, pH 8.0 for 6-His tagged protein).

nAChR Co-immunoprecipitation: HEK293 cells (1 x 10^6 cells/transfection) were co-transfected with pLynx1-mCherry and four nAChR subunits (α, β, δ and ε). At 36 h post-transfection cell lysates were obtained following addition of ice cold lysis buffer (50 mM Tris-HCl, 150 mM NaCl, 50 mM NaH2PO4, 10 mM Imidazole, 0.1% NP40, 10% glycerol,

protease inhibitor cocktail, and 50mM DTT, pH 8), incubation on a rotary shaker (1h, 4°C), and centrifugation at 13,000 x g at 4°C. The immunoprecipitation was performed as previously described(*65*). Briefly, the lysates were centrifuged, and supernatants were incubated with Dynabeads (Invitrogen, #10003D) and coated with anti-AChR antibody (Biolegend, #838301). Beads were then washed three times with lysis buffer, resuspended in 2x sample buffer (4% SDS, 20% glycerol, 200mM DTT, 0.01% bromophenol blue, 200mM DTT, 20% glycerol) and boiled for 5 min. The samples were resolved by SDS-PAGE electrophoresis and analyzed with anti-AChR antibody (Biolegend, #838301) and anti-red fluorescent protein (RFP) antibody (Rockland, #600-401-379), which cross-reacts with mCherry and other RFP variants.

nAChR ectodomain pull-down assays: To coat glutathione beads with purified GST-tagged truncated nAChR subunits (α, β, δ, ε, and γ), the glutathione beads and purified GST-tagged truncated nAChR subunits were incubated overnight at 4°C in in 1X PBS containing 1% NP40, 2 mM DTT, and Protease inhibitor (Roche #4693159001). These were washed three times with washing buffer (50 mM Tris-HCl, 150 mM NaCl, 50 mM NaH2PO4, 10 mM Imidazole, 0.1% NP40, pH 8, with protease inhibitor cocktail), followed by addition of homogenates of HEK293 cells transfected with pLynx1-Cherry, and then incubated overnight at 4°C. The beads were washed with washing buffer and boiled with 2x sample buffer. The precipitated proteins were resolved by SDS-PAGE electrophoresis and detected with anti-RFP or anti-GST (Cat No: G7781, Sigma, St. Louis, MO) antibodies.

To determine the direct interaction of GST-Lynx1 with the extracellular domain of the nAChR α subunit, the truncated GST-tagged nAChR α ectodomain was incubated with

BTX-biotin coated (Thermo Fisher Scientific, #B1196) Streptavidin Dynabeads (Thermo Fisher Scientific, # 11205D) for one hour at 4°C. Beads were then washed three times with lysis buffer, and incubated with the purified GST-Lynx1 overnight. Beads were then washed three times with lysis buffer, resuspended in 2x sample buffer and boiled for 5 min. The samples were resolved by SDS-PAGE electrophoresis and analyzed with anti-GST antibody.

For analysis of 6XHis-tagged Lynx1 specificity for AChR subunits, 20 µl glutathione beads were coated with purified GST-tagged AChR subunits as described above. These beads were washed three times with washing buffer, followed by incubation with the purified 6-His-Lynx1 overnight. The beads were washed with washing buffer and eluted with elution buffer (10 mM glutathione 50 mM Tris pH=8,0). The eluted proteins were mixed with 2x sample buffer and were resolved by SDS-PAGE electrophoresis and detected with anti-His (Proteintech, #66005-1-Ig) or anti-GST (Sigma #G7781,) antibodies.

Lynx1 antibody generation

An antibody against Lynx1 was developed following the methods previously outlined (*66*). In brief, a piggyback transposon vector pXL-CAG-Zeomycin-2A and a piggyback transposase vector pCAG-mPBorf were obtained as a gift from Dr. Joshua Sanes. The Lynx1 sequence was cloned into the transposon vector following the 2A peptide sequence. L-cells were co-transfected with pXL-CAG-Zeomycin-2A-Lynx1 and pCAG-mPBorf. A stable cell line of Lynx1-expressing L-cells was generated by selection with Zeomycin and expression analysis confirmed the presence of Lynx1 mRNA. An antibody against mouse Lynx1 was generated by immunizing 1 mo. Lynx1$^{-/-}$ mice with Lynx1-expressing L cells. Total serum was collected from immunized mice after six weeks of

immunizations and purified using acetone powder. Antibody specificity was verified using transfected L cells and knockout mouse tissue (Fig. 1E).

Electrophysiology recordings

Nerve-muscle preparations: Nerve–muscle preparations of the EDL muscle were dissected in oxygenated physiological solution (in mM): 110 NaCl, 5 KCl, 1 MgCl2, 25 NaHCO3, 2 CaCl2, 11 glucose, 0.3 glutamic acid, 0.4 glutamine, 5 BES (N,N-Bis(2-hydroxyethyl)-2-aminoethanesulfonic acid sodium salt), 0.036 choline chloride, and 4.34x10-7 cocarboxylase. After dissection, nerve muscle preparations were pinned in a Sylgard-coated recording chamber constantly perfused with oxygenated physiological solution (95%O2, 5%CO2). The pH (7.4) and temperature (28 ±2°C) were continuously regulated.

Recordings of synaptic transmission: Only recordings with an initial membrane potential larger than -65 mV and with less than 5 mV variation from holding potential were included in the analysis. NMJs were located using bright field illumination of an upright Olympus microscope with a 60X objective. Muscle fibers were impaled 50-100 µm from the NMJ to be studied, avoiding mechanical distortion of the NMJ.

Stimulation of the deep peroneal nerve was performed using a suction electrode filled with extracellular saline. Endplate potentials (EPPs) were recorded using glass microelectrodes (1.0 mm OD; WPI) pulled to 40-70 MΩ (filled with 3mM KCl) with a P-70 Brown-Flaming micropipette puller (Sutter Instruments). Synaptic responses were amplified by an AM Systems 1600 amplifier and further amplified (100x) and filtered (2 kHz) by a Warner Instruments DC amplifier. The recordings were digitized (10 KHz) using

a National Instruments BNC 2110 board and subsequently acquired with WinWCP software (John Dempster, Strathclyde University, Strathclyde, UK).

Synaptic strength was determined by measuring the paired pulse facilitation (PPF) and the quantal content (m). These were obtained using a low Ca^{2+} (1mM) and high Mg^{2+} (7.0mM) modified physiological solution. Miniature endplate potentials (MEPPs) amplitude and frequency were first determined during a 5-10 min period of recordings without motor nerve stimulation. PPF was then obtained using two stimuli (0.1 ms duration, 10 ms interval), elicited at 0.2 Hz. Quantal content (m) was determined using the amplitude of the first EPP (EPP1) and MEPPs (mean EPP1s amp/mean MEPPs amp). Four to seven NMJs were studied per muscle.

Following a baseline recording of 20 min (0.2 Hz), synaptic plasticity was elicited by a sustained motor nerve stimulation (120 Hz, 10 s) followed by 45 min recordings of EPPs evoked at 0.2 Hz. Muscle contractions were prevented with partial blockade of the postsynaptic ACh receptors using D-tubocurarine (2.0 µM. Sigma). Only one NMJ was studied per muscle.

Muscular strength and fatigue: EDL nerve-muscle preparations were attached to a fixed force transducer (model 402A-500mN, Aurora Scientific Inc) at one end and an adjustable hook at the other end, using surgical thread. The knots for attaching the muscle to the force transducer and the hook were done at the level of the tendons, under a binocular, to prevent muscle fiber damage. Muscles were maintained vertically in a 140 ml beaker containing oxygenated physiological solution. Two platinum wires were positioned on the muscle and on the tendon to stimulate the muscle directly.

Muscular twitch force responses were elicited by means of single supra-maximal square-wave pulses lasting 1 ms and 0.1 ms, respectively. Optimal muscle length was determined by incrementally stretching the muscle until maximum neuro-muscular twitch force output was attained. After each length adjustment, a two-minute rest period was allowed before the next stimulation.

The fatigue protocol consisted of bouts of motor nerve stimulations (120Hz, 300 ms) at 1Hz, for 3 min. Muscular stimulations were combined with nerve stimulations (data not shown) at the 2nd and 10th stimulation, and every 10th stimulation thereafter until the end of the fatigue protocol. This was followed by a 30 min recovery period where muscular and strength was measured at 2s, 5s, 10s, 15s, 30s, 1min, 1.5 min, 2 min, 2.5 m in, 5 min, 10 min, 20 min and 30 min following the fatigue protocol.

Immunohistochemistry and confocal microscopy of EDL muscles

EDL muscles from Thy1-YFP16 mice expressing YFP in nerve endings were used to visualize NMJs. Following perfusion, muscles were dissected and incubated with Alexa Fluor 555 conjugated BTX (Invitrogen, #B35451, 1:1000 in 1XPBS) for 1 hour. Muscles were then washed 3 times with 1X PBS and whole mounted in vectashield (Vector Laboratories). For Lynx1 IHC, EDL muscles were incubated 1 hour at room temperature in blocking buffer (1X PBS, 5% bovine serum albumin, 3% goat serum, 0.5% Triton-X), incubated overnight at 4°C in Lynx1 antibody diluted 1:10 in blocking buffer, washed 3 times with 1X PBS, incubated 2 h at room temperature in Alexa Fluor 488 conjugated polyclonal anti-mouse IgG antibody (Invitrogen # A-11001, 1:1000) and Alexa Fluor 555 conjugated BTX (1:1000) diluted in blocking buffer, washed 3 times with 1X PBS, and whole mounted in vectashield NMJs were imaged using a Zeiss LSM 700 confocal

microscope. Maximum intensity projections from confocal z-stacks were created using Zen Black software (Zeiss).

NMJ analysis: Structural features were analyzed based on previously described methods (*44*). In brief, full or partial denervation of NMJs was classified by inadequate apposition of YFP labeled motor axon terminal with fluorescently conjugated BTX (fBTX) labeled nAChR cluster. Fragmented nAChRs were defined as having 5 or more islands in the cluster. Sprouting NMJs were those with a nerve terminal overreaching the nAChR cluster. NMJs with multiple innervation were those with more than one axon innervating a single nAChR cluster. The endplate area was a measurement of the total area occupied by nAChR clusters in a single muscle. Colocalization was a measurement of YFP and fBTX apposition analyzed using the ImageJ colocalization plugin. nAChR intensity was measured using ImageJ by calculating the corrected total cell fluorescence (CTCF). The corrected value was determined by multiplying the area of each NMJ by the average background fluorescence intensity. The CTCF was then calculated by subtracting the corrected value from the integrated density of each NMJ.

Lynx1 intensity analysis: Lynx1 NMJ intensity analysis was performed on confocal images of EDL muscles following Lynx1 and fBTX IHC. NMJs were delineated by fBTX-labeled nAChRs. Calculations of Lynx1 and fBTX signal colocalization were used to determine Lynx1 signal intensity at NMJs. The ImageJ Coloc2 function was used to determine Pearson's R coefficient between the Lynx1 and fBTX channel for each nAChR outlined. At least 100 nAChRs were analyzed per muscle, the average Pearson's R coefficient for each group is plotted.

Immunohistochemistry and confocal microscopy of TA sections

PFA-fixed TA muscles were dissected and incubated in 30% sucrose for 48 hours at 4°C. Muscles were then cut in half and placed in base molds (Fisherbrand) with Tissue Freezing Medium (General Data Healthcare). Using a cryostat, TA muscles were cross-sectioned at 16 µm thickness and collected on gelatin-coated slides. Sections were first washed 3 times with 1XPBS and then incubated for 1 hour at room temperature with wheat germ agglutinin conjugated with Alexa Fluor 555 (WGA, 1:700) and DAPI (4'6-diamidino-2-phenylindole: Sigma-Aldrich; 28718-90-3; 1:1,000) diluted in 1XPBS. Muscles were then washed 3 times with 1XPBS and whole mounted using vectashield (Vector Laboratories). Muscle fibers were imaged using a Zeiss LSM 700 confocal microscope using a 20X objective (0.8 numerical aperture). Maximum intensity projections from confocal z-stacks were created using Zen Black (Zeiss) and analyzed using ImageJ. Muscle fiber perimeters were identified by WGA and measured in ImageJ using the grid to randomly select at least 100 fibers per mouse. Muscle fibers with centralized nuclei were identified by presence of a DAPI-labeled nucleus near its center.

qPCR expression analysis

Mice were anesthetized with isoflurane, and TA muscles were immediately dissected and flash frozen in liquid nitrogen. RNA was isolated using an Aurum Total RNA Mini kit (Bio-Rad), following the manufacturer's instructions. cDNA was then synthesized from 100 ng of total RNA using an iScript cDNA synthesis kit (Bio-Rad). qPCR was performed on the Bio-Rad CFX Connect Real-Time System (Bio-Rad) using iTaq Universal SYBR Green Supermix (Bio-Rad). The primers used in this study are listed in Table 1.

nAChR turnover analysis

The labeling of distinct nAChR pools was performed as described in Bruneau et al.(*40*) with slight modifications. Male C57/BL6 and Lynx1$^{-/-}$ mice, aged 148 days, were anesthetized by an intraperitoneal injection (5µL/g) of a mixed solution of ketamine (100mg/mL) and xylazine (20mg/mL) in sterile 0.9% saline. Each mouse was placed on its back and the sternomastoid muscle was surgically exposed. Muscles were bathed in saturating levels of Alexa Fluor 488 conjugated α-bungarotoxin (5µg/mL) for 1.5 h and then washed with sterile saline 3 times for 5 minutes. Two days following exposure, the animals were perfused transcardially with 4% PFA and the sternomastoid muscles were dissected. Muscles were then incubated with Alexa Fluor 555 conjugated α-bungarotoxin ((Invitrogen, #B35451, 5µg/mL) for 1.5 h and washed with sterile saline 3 times for 5 minutes each. Whole Sternomastoid muscles were mounted using vectashield and imaged with a Zeiss LSM 710 confocal microscope. Maximum intensity projections from confocal z-stacks were created using Zen Black (Zeiss). Alexa Fluor 488 and 555 signal intensities were analyzed at individual NMJs using ImageJ. The ratio of 555 to overall intensity was calculated for each NMJ and averaged for each animal. This ratio is considered the percentage of new nAChRs present.

Statistics

For comparisons between two experimental groups, unpaired two-sided Student's t-tests were used to determine significance. For comparisons of two independent variables, two-way ANOVA with Bonferroni post-hoc was used to determine significance. For comparisons between two sample distributions, Kolmogorov–Smirnov tests were used to determine significance. Bar graphs are represented as means ± standard error. P-values

and sample sizes (*n*) are described in the figure legends. A p-value < 0.05 was considered statistically significant. Statistical analysis was performed using R statistics software and GraphPad Prism7.

References

1. G. W. Davis, Homeostatic signaling and the stabilization of neural function. *Neuron*. **80** (2013), pp. 718–728.

2. L. F. Abbott, S. B. Nelson, Synaptic plasticity: Taming the beast. *Nat. Neurosci.* **3**, 1178–1183 (2000).

3. P. R. Roelfsema, A. Holtmaat, Control of synaptic plasticity in deep cortical networks. *Nat. Rev. Neurosci.* **19** (2018), pp. 166–180.

4. X. Wang, M. M. Rich, Homeostatic synaptic plasticity at the neuromuscular junction in myasthenia gravis. *Ann. N. Y. Acad. Sci.* **1412**, 170–177 (2018).

5. R. J. Balice-Gordon, J. W. Lichtman, In vivo visualization of the growth of pre- and postsynaptic elements of neuromuscuolar junctions in the mouse. *J. Neurosci.* **10**, 894–908 (1990).

6. H. Darabid, A. P. Perez-Gonzalez, R. Robitaille, Neuromuscular synaptogenesis: coordinating partners with multiple functions. *Nat. Rev. Neurosci.* **15**, 703–18 (2014).

7. Z. W. Hall, J. R. Sanes, Synaptic structure and development: The neuromuscular junction. *Cell*. **72** (1993), pp. 99–121.

8. J. R. Sanes, J. W. Lichtman, Development of the vertebrate neuromuscular

junction. *Annu. Rev. Neurosci.* **22**, 389–442 (1999).

9. T. Taetzsch, G. Valdez, NMJ maintenance and repair in aging. *Curr. Opin. Physiol.* **4**, 57–64 (2018).

10. D. Arbour, E. Tremblay, E. Martineau, J.-P. Julien, R. Robitaille, Early and Persistent Abnormal Decoding by Glial Cells at the Neuromuscular Junction in an ALS Model. *J. Neurosci.* **35**, 688–706 (2015).

11. M. C. Rocha, P. A. Pousinha, A. M. Correia, A. M. Sebastião, J. A. Ribeiro, Early changes of neuromuscular transmission in the SOD1(G93A) mice model of ALS start long before motor symptoms onset. *PLoS One*. **8**, e73846 (2013).

12. P. A. Pousinha, A. M. Correia, A. M. Sebastião, J. A. Ribeiro, The giant miniature endplate potentials frequency is increased in aged rats. *Neurosci. Lett.* **584**, 224–229 (2015).

13. E. B. Moloney, F. de Winter, J. Verhaagen, ALS as a distal axonopathy: molecular mechanisms affecting neuromuscular junction stability in the presymptomatic stages of the disease. *Front. Neurosci.* **8**, 252 (2014).

14. T. Misgeld, T. T. Kummer, J. W. Lichtman, J. R. Sanes, Agrin promotes synaptic differentiation by counteracting an inhibitory effect of neurotransmitter. *Proc. Natl. Acad. Sci. U. S. A.* **102**, 11088–93 (2005).

15. T. Misgeld, R. W. Burgess, R. M. Lewis, J. M. Cunningham, J. W. Lichtman, J. R. Sanes, Roles of neurotransmitter in synapse formation: development of neuromuscular junctions lacking choline acetyltransferase. *Neuron*. **36**, 635–48

(2002).

16. M. A. Lanuza, N. Besalduch, C. González, M. M. Santafé, N. Garcia, M. Tomàs, P. G. Nelson, J. Tomàs, Decreased phosphorylation of delta and epsilon subunits of the acetylcholine receptor coincides with delayed postsynaptic maturation in PKC theta deficient mouse. *Exp. Neurol.* **225**, 183–195 (2010).

17. A. G. M. Leenders, Z.-H. Sheng, Modulation of neurotransmitter release by the second messenger-activated protein kinases: implications for presynaptic plasticity. *Pharmacol. Ther.* **105**, 69–84 (2005).

18. D. O. Smith, K. D. Williams, M. Emmerling, Changes in acetylcholine receptor distribution and binding properties at the neuromuscular junction during aging. *Int. J. Dev. Neurosci.* **8**, 629–42 (1990).

19. M. B. Friese, C. S. Blagden, S. J. Burden, Synaptic differentiation is defective in mice lacking acetylcholine receptor β-subunit tyrosine phosphorylation. *Development*. **134**, 4167–4176 (2007).

20. J. M. Miwa, J. M. Miwa, I. Ibanez-Tallon, I. Ibanez-Tallon, G. W. Crabtree, G. W. Crabtree, R. Â€¦, R. Â€¦, lynx 1, an Endogenous Toxin-like Modulator of Nicotinic Acetylcholine Receptors in the â€¦. *Neuron*. **23**, 0 (1999).

21. I. Ibanez-Tallon, J. M. Miwa, H. L. Wang, N. C. Adams, G. W. Crabtree, S. M. Sine, N. Heintz, I. Ibañez-Tallon, J. M. Miwa, H. L. Wang, N. C. Adams, G. W. Crabtree, S. M. Sine, N. Heintz, Novel modulation of neuronal nicotinic acetylcholine receptors by association with endogenous prototoxin lyn1. *Neuron*. **33**, 893–903 (2002).

22. E. N. Lyukmanova, M. A. Shulepko, S. L. Buldakova, I. E. Kasheverov, Z. O. Shenkarev, R. V. Reshetnikov, S. Y. Filkin, D. S. Kudryavtsev, L. O. Ojomoko, E. V. Kryukova, D. A. Dolgikh, M. P. Kirpichnikov, P. D. Bregestovski, V. I. Tsetlin, Water-soluble LYNX1 Residues Important for Interaction with Muscle-type and/or Neuronal Nicotinic Receptors. *J. Biol. Chem.* **288**, 15888–15899 (2013).

23. W. A. Nichols, B. J. Henderson, C. Yu, R. L. Parker, C. I. Richards, H. A. Lester, J. M. Miwa, Lynx1 Shifts 4 2 Nicotinic Receptor Subunit Stoichiometry by Affecting Assembly in the Endoplasmic Reticulum. *J. Biol. Chem.* **289**, 31423–31432 (2014).

24. A. A. George, A. Bloy, J. M. Miwa, J. M. Lindstrom, R. J. Lukas, P. Whiteaker, Isoform-specific mechanisms of α3β4*-nicotinic acetylcholine receptor modulation by the prototoxin lynx1. *FASEB J.* **31**, 1398–1420 (2017).

25. E. M. Nabel, H. Morishita, Regulating Critical Period Plasticity: Insight from the Visual System to Fear Circuitry for Therapeutic Interventions. *Front. Psychiatry*. **4**, 146 (2013).

26. H. Morishita, J. M. Miwa, N. Heintz, T. K. Hensch, Lynx1, a cholinergic brake, limits plasticity in adult visual cortex. *Science*. **330**, 1238–40 (2010).

27. A. E. Takesian, L. J. Bogart, J. W. Lichtman, T. K. Hensch, Inhibitory circuit gating of auditory critical-period plasticity. *Nat. Neurosci.* **21**, 218–227 (2018).

28. J. M. Miwa, A. Walz, Enhancement in Motor Learning through Genetic Manipulation of the Lynx1 Gene. *PLoS One*. **7** (2012), doi:10.1371/.

29. R. L. Parker, H. C. O'Neill, B. M. Henley, C. R. Wageman, R. M. Drenan, M. J.

Marks, J. M. Miwa, S. R. Grady, H. A. Lester, Deletion of lynx1 reduces the function of α6* nicotinic receptors. *PLoS One*. **12**, e0188715 (2017).

30. N. I. Nissen, K. R. Anderson, H. Wang, H. S. Lee, C. Garrison, S. A. Eichelberger, K. Ackerman, W. Im, J. M. Miwa, Augmenting the antinociceptive effects of nicotinic acetylcholine receptor activity through lynx1 modulation. *PLoS One*. **13** (2018), doi:10.1371/journal.pone.0199643.

31. J. M. Miwa, T. R. Stevens, S. L. King, B. J. Caldarone, I. Ibanez-Tallon, C. Xiao, R. M. Fitzsimonds, C. Pavlides, H. A. Lester, M. R. Picciotto, N. Heintz, The Prototoxin lynx1 Acts on Nicotinic Acetylcholine Receptors to Balance Neuronal Activity and Survival In Vivo. *Neuron*. **51**, 587–600 (2006).

32. A. Kobayashi, R. L. Parker, A. P. Wright, H. Brahem, P. Ku, K. M. Oliver, A. Walz, H. A. Lester, J. M. Miwa, lynx1 Supports Neuronal Health in the Mouse Dorsal Striatum During Aging: an Ultrastructural Investigation. *J. Mol. Neurosci.* **53**, 525–536 (2014).

33. M. S. Thomsen, M. Arvaniti, M. M. Jensen, M. A. Shulepko, D. A. Dolgikh, L. H. Pinborg, W. Härtig, E. N. Lyukmanova, J. D. Mikkelsen, Lynx1 and Aβ1-42 bind competitively to multiple nicotinic acetylcholine receptor subtypes (2016), doi:10.1016/j.neurobiolaging.2016.06.009.

34. M. R. Celio, C. W. Heizmann, Calcium-binding protein parvalbumin is associated with fast contracting muscle fibres. *Nature*. **297**, 504–6 (1982).

35. S. Hippenmeyer, E. Vrieseling, M. Sigrist, T. Portmann, C. Laengle, D. R. Ladle, S. Arber, A developmental switch in the response of DRG neurons to ETS

transcription factor signaling. *PLoS Biol.* **3**, e159 (2005).

36. E. Sanz, L. Yang, T. Su, D. R. Morris, G. S. McKnight, P. S. Amieux, Cell-type-specific isolation of ribosome-associated mRNA from complex tissues. *Proc. Natl. Acad. Sci. U. S. A.* **106**, 13939–44 (2009).

37. T. T. Kummer, T. Misgeld, J. W. Lichtman, J. R. Sanes, Nerve-independent formation of a topologically complex postsynaptic apparatus. *J. Cell Biol.* **164**, 1077–87 (2004).

38. C. D. Dellisanti, Y. Yao, J. C. Stroud, Z. Z. Wang, L. Chen, Crystal structure of the extracellular domain of nAChR α1 bound to α-bungarotoxin at 1.94 Å resolution. *Nat. Neurosci.* **10**, 953–962 (2007).

39. E. N. Lyukmanova, Z. O. Shenkarev, M. A. Shulepko, K. S. Mineev, D. D'Hoedt, I. E. Kasheverov, S. Y. Filkin, A. P. Krivolapova, H. Janickova, V. Dolezal, D. A. Dolgikh, A. S. Arseniev, D. Bertrand, V. I. Tsetlin, M. P. Kirpichnikov, NMR structure and action on nicotinic acetylcholine receptors of water-soluble domain of human LYNX1. *J. Biol. Chem.* **286**, 10618–10627 (2011).

40. E. Bruneau, D. Sutter, R. I. Hume, M. Akaaboune, Identification of Nicotinic Acetylcholine Receptor Recycling and Its Role in Maintaining Receptor Density at the Neuromuscular Junction In Vivo (2005), doi:10.1523/JNEUROSCI.3169-05.2005.

41. J. Courtney, J. H. Steinbach, Age changes in neuromuscular junction morphology and acetylcholine receptor distribution on rat skeletal muscle fibres. *J. Physiol.* **320**, 435–47 (1981).

42. A. Cheng, M. Morsch, Y. Murata, N. Ghazanfari, S. W. Reddel, W. D. Phillips, Sequence of Age-Associated Changes to the Mouse Neuromuscular Junction and the Protective Effects of Voluntary Exercise. *PLoS One* (2013), doi:10.1371/journal.pone.0067970.

43. Y. Li, Y. il Lee, W. J. Thompson, Changes in aging mouse neuromuscular junctions are explained by degeneration and regeneration of muscle fiber segments at the synapse. *J. Neurosci.* **31**, 14910–9 (2011).

44. G. Valdez, J. C. Tapia, H. Kang, G. D. Clemenson Jr., F. H. Gage, J. W. Lichtman, J. R. Sanes, Attenuation of age-related changes in mouse neuromuscular synapses by caloric restriction and exercise. *Proc Natl Acad Sci U S A*. **107**, 14863–14868 (2010).

45. E. S. Folker, M. K. Baylies, Nuclear positioning in muscle development and disease. *Front. Physiol.* **4 DEC** (2013), , doi:10.3389/fphys.2013.00363.

46. G. Valdez, J. C. Tapia, H. Kang, G. D. Clemenson, F. H. Gage, J. W. Lichtman, J. R. Sanes, G. D. Clemenson Jr., F. H. Gage, J. W. Lichtman, J. R. Sanes, G. D. Clemenson, F. H. Gage, J. W. Lichtman, J. R. Sanes, Attenuation of age-related changes in mouse neuromuscular synapses by caloric restriction and exercise. *Proc. Natl. Acad. Sci. U. S. A.* **107**, 14863–8 (2010).

47. M. Sajo, G. Ellis-Davies, H. Morishita, Lynx1 Limits Dendritic Spine Turnover in the Adult Visual Cortex. *J. Neurosci.* **36**, 9472–8 (2016).

48. W. Dalkin, T. Taetzsch, G. Valdez, The Fibular Nerve Injury Method: A Reliable Assay to Identify and Test Factors That Repair Neuromuscular Junctions. *J. Vis.*

Exp. (2016), doi:10.3791/54186.

49. J. Stockinger, N. Maxwell, D. Shapiro, R. deCabo, G. Valdez, Caloric Restriction Mimetics Slow Aging of Neuromuscular Synapses and Muscle Fibers. *Journals Gerontol. Ser. A* (2017), doi:10.1093/gerona/glx023.

50. G. Valdez, J. C. Tapia, H. Kang, G. D. Clemenson, F. H. Gage, J. W. Lichtman, J. R. Sanes, Attenuation of age-related changes in mouse neuromuscular synapses by caloric restriction and exercise. *Proc. Natl. Acad. Sci. U. S. A.* **107**, 14863–8 (2010).

51. S. Sugita, L. L. Fleming, C. Wood, S. K. Vaughan, M. P. S. M. Gomes, W. Camargo, L. A. Naves, V. F. Prado, M. A. M. Prado, C. Guatimosim, G. Valdez, VAChT overexpression increases acetylcholine at the synaptic cleft and accelerates aging of neuromuscular junctions. *Skelet. Muscle*. **6**, 31 (2016).

52. B. Q. Banker, S. S. Kelly, N. Robbins, Neuromuscular transmission and correlative morphology in young and old mice. *J. Physiol.* **339**, 355–77 (1983).

53. S. S. Kelly, The effect of age on neuromuscular transmission. *J. Physiol.* **274**, 51–62 (1978).

54. E. Tremblay, É. Martineau, R. Robitaille, Opposite Synaptic Alterations at the Neuromuscular Junction in an ALS Mouse Model: When Motor Units Matter. *J. Neurosci.* **37**, 8901–8918 (2017).

55. P. A. Pousinha, A. M. Correia, A. M. Sebastião, J. A. Ribeiro, The giant miniature endplate potentials frequency is increased in aged rats. *Neurosci. Lett.* **584**, 224–9

(2015).

56. S. Willadt, M. Nash, C. Slater, Age-related changes in the structure and function of mammalian neuromuscular junctions. *Ann. N. Y. Acad. Sci.* **1412**, 41–53 (2018).

57. J. M. Venuti, J. H. Morris, J. L. Vivian, E. N. Olson, W. H. Klein, Myogenin is required for late but not early aspects of myogenesis during mouse development. *J. Cell Biol.* **128**, 563–576 (1995).

58. J. R. Sanes, J. W. Lichtman, Induction, assembly, maturation and maintenance of a postsynaptic apparatus. *Nat. Rev. Neurosci.* **2**, 791–805 (2001).

59. Y. S. Liu, M. Fujita, Mammalian GPI-anchor modifications and the enzymes involved. *Biochem. Soc. Trans.* **48** (2020), pp. 1129–1138.

60. T. Taetzsch, M. J. Tenga, G. Valdez, Muscle Fibers Secrete FGFBP1 to Slow Degeneration of Neuromuscular Synapses during Aging and Progression of ALS. *J. Neurosci.* **37**, 70–82 (2017).

61. P. C. D. Macpherson, P. Farshi, D. Goldman, Dach2-Hdac9 signaling regulates reinnervation of muscle endplates. *Dev.* **142**, 4038–4048 (2015).

62. G. Valdez, M. P. Heyer, G. Feng, J. R. Sanes, The role of muscle microRNAs in repairing the neuromuscular junction. *PLoS One*. **9**, e93140 (2014).

63. G. Feng, R. H. Mellor, M. Bernstein, C. Keller-Peck, Q. T. Nguyen, M. Wallace, J. M. Nerbonne, J. W. Lichtman, J. R. Sanes, Imaging Neuronal Subsets in Transgenic Mice Expressing Multiple Spectral Variants of GFP. *Neuron*. **28**, 41–51 (2000).

64. D. Herrmann, M. Straubinger, S. Hashemolhosseini, Protein kinase CK2 interacts at the neuromuscular synapse with Rapsyn, Rac1, 14-3-3γ, and Dok-7 proteins and phosphorylates the latter two. *J. Biol. Chem.* (2015), doi:10.1074/jbc.M115.647610.

65. J. Gingras, M. Gawor, K. M. Bernadzki, R. M. Grady, P. Hallock, D. J. Glass, J. R. Sanes, T. J. Proszynski, α-Dystrobrevin-1 recruits Grb2 and α-catulin to organize neurotransmitter receptors at the neuromuscular junction. *J. Cell Sci.* (2016), doi:10.1242/jcs.181180.

66. K. M. Goodman, M. Yamagata, X. Jin, S. Mannepalli, P. S. Katsamba, G. Ahlsén, A. P. Sergeeva, B. Honig, J. R. Sanes, L. Shapiro, Molecular basis of sidekick-mediated cell-cell adhesion and specificity. *Elife*. **5**, e19058 (2016).

Acknowledgements

Funding

This work was funded through grants from the National Institute on Aging (R01AG055545 and R56AG051501) and the National Institute of Neurological Disorders and Stroke (R21NS106313) awarded to GV.

Author Contributions

Conceptualization, G.V. and S.D.; Methodology, Writing-Original Draft, and Validation, S.D., T.P., R.R., and G.V.; Investigation and Formal Analysis, S.D., S.B., T.M., B.P., T.P. and R.R.; Writing- Reviewing & Editing, S.D., S.B., T.M., B.P., T.M., R.R., and G.V.; Data Curation and Visualization, S.D.; Resources, Supervision, and Funding Acquisition, T.P.,

R.R., and G.V.; Project Administration, G.V. Work was performed in the laboratories of T.P., R.R., and G.V.

Competing Interests

The authors have no competing interests to declare.

Figures and Tables

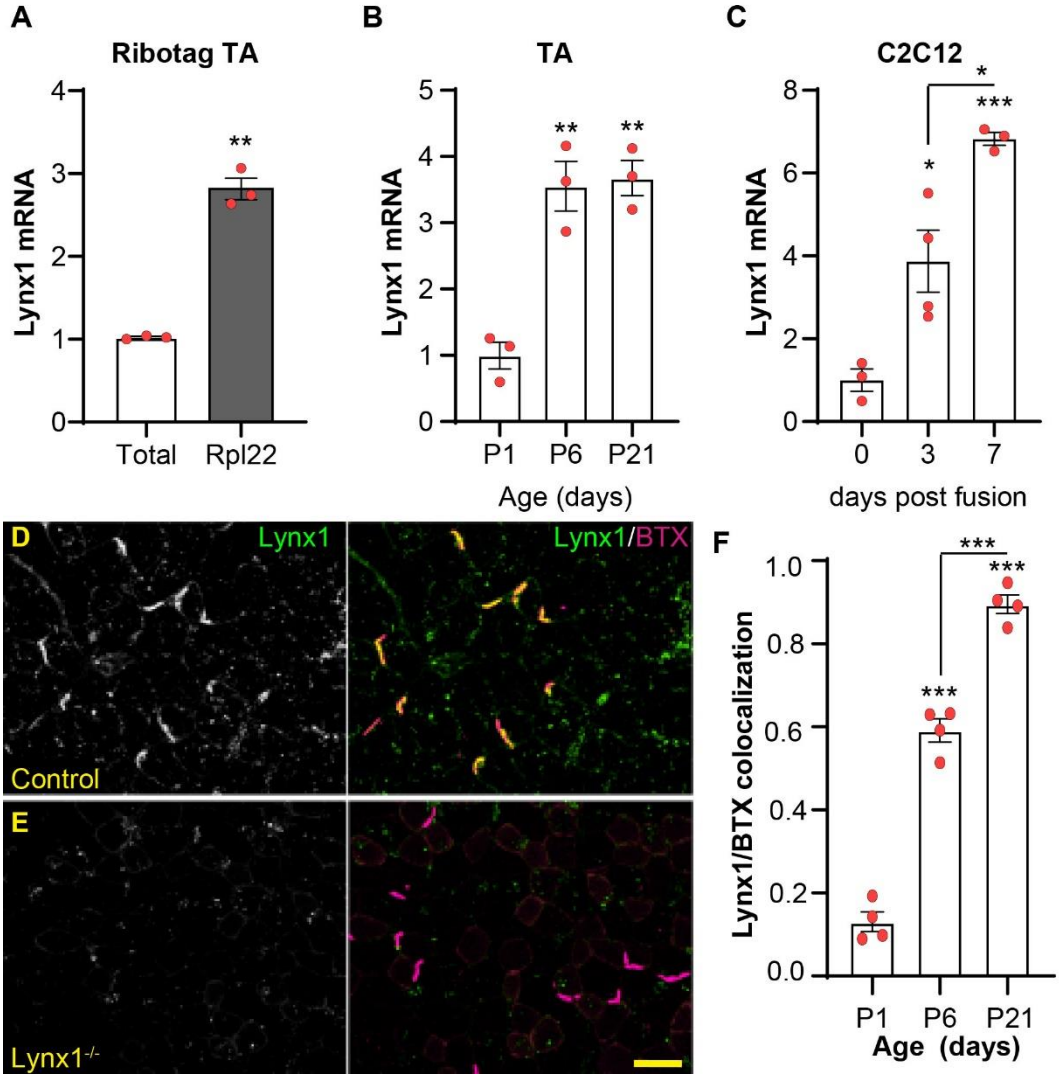

Figure 1. Skeletal muscles express Lynx1 at the NMJ. (A) qPCR analysis of Lynx1 mRNA levels in whole cell lysate (Total) versus ribosome-associated mRNA fractions immunoprecipitated from HA-tagged Rpl22 expressed specifically in fast twitch skeletal muscle fibers (Rpl22) in adult TA muscle of 3 mo. PVCre; RiboTag$^{flox/flox}$ mice (n = 4). (B) Lynx1 mRNA expression is detected in TA and EDL muscles by qPCR and is significantly upregulated at P6 and P21, relative to P1 (n = 5). (C) Lynx1 mRNA is expressed in C2C12 myotubes and is significantly upregulated at 3 and 7 days post-fusion compared to unfused myoblasts, as assessed by qPCR (n ≥ 3). (D-E) Representative images of Lynx1 (green) and fBTX labeled nAChRs (magenta) in control (D) and Lynx1$^{-/-}$ (E) TA muscle cross-sections show an absence of Lynx1 colocalization with nAChRs in Lynx1-/- muscles. (F) In control muscles, Lynx1 colocalization with fBTX is significantly increased at P6 and P21, relative to P1 (n = 4). Data represented as mean ± SEM. qPCR expression is normalized to GAPDH using the $2^{-\Delta\Delta CT}$ method. Scale bar = 20 µm. Statistical significance was determined with unpaired and two-sided Student's t-tests. *p<0.05, **p<0.01, ***p<0.001.

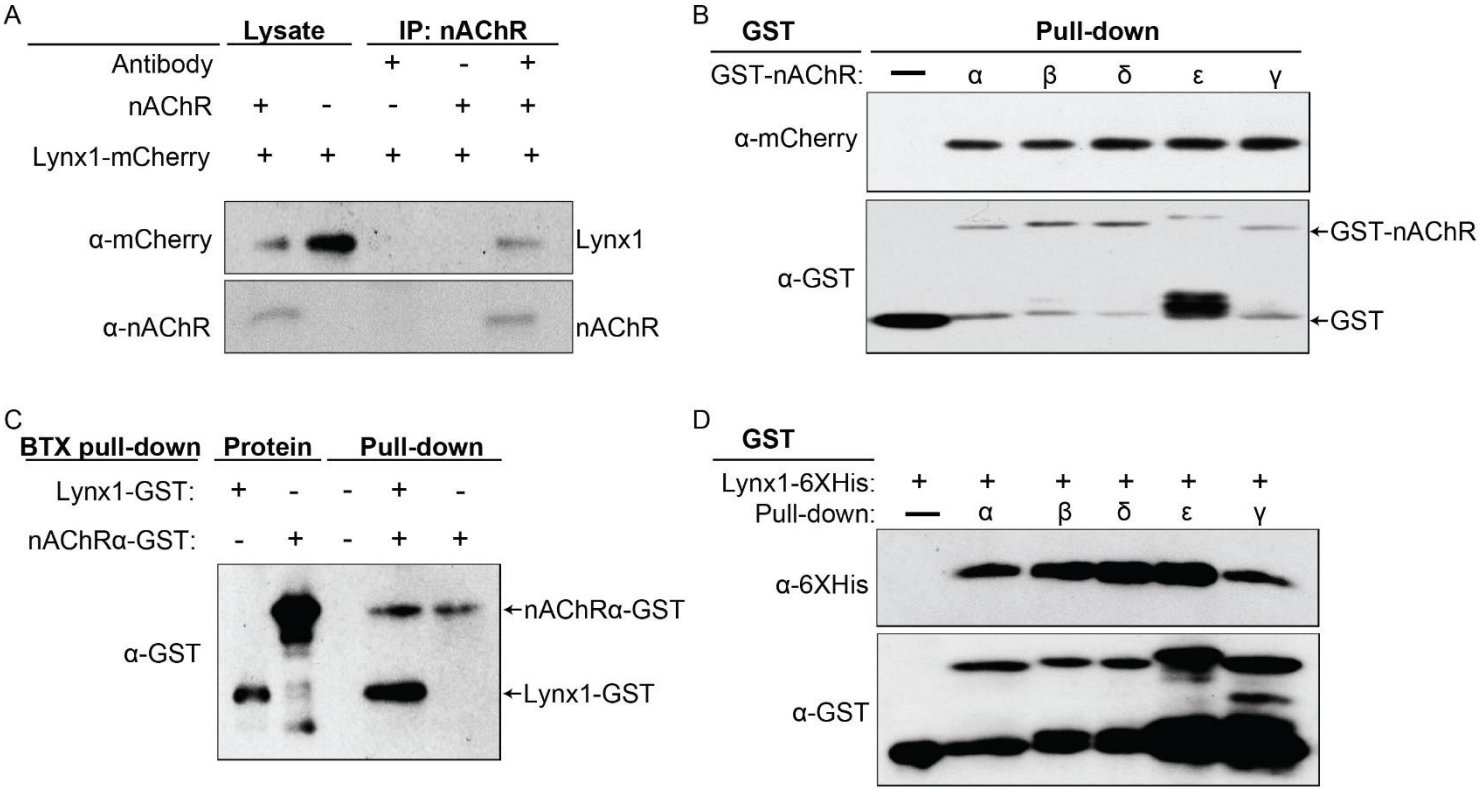

Figure 2. Lynx1 interacts with nAChRs. (A) nAChR CO-IP of HEK293 cells co-transfected with Lynx1-mCherry and the α1, β1, δ and ε nAChR subunits. Western blot was performed with anti-mCherry or anti-nAChR antibodies. Lane 1, cell lysate transfected with Lynx1-mCherry and nAChR subunits. Lane 2, cell lysate transfected with Lynx1-mCherry only. Lane 3, nAChR CO-IP of cell lysate transfected with Lynx1-mCherry only. Lane 4, no antibody CO-IP of cell lysate transfected with Lynx1-mCherry and nAChR subunits. Lane 5, nAChR CO-IP of cell lysate transfected with Lynx1-mCherry and nAChR subunits. (B) GST pull-down assay of HEK293 cell lysate following transfection with Lynx1-mCherry. (Upper image) mCherry Western blot revealed that Lynx1-mCherry was pulled down by GST-tagged α1, β1, δ, ε, or γ nAChR subunit ectodomains but not by GST alone (left lane). (Lower image) GST Western blot revealed GST-tagged nAChR subunit ectodomains at the predicted sizes. (C) BTX pull-down of purified recombinant GST-tagged truncated α1 nAChR and GST-tagged Lynx1. Western blot was performed with a GST antibody. Lanes 1 and 2 show GST-tagged Lynx1 and GST-tagged truncated α1 nAChR at their predicted sizes. Lanes 3-5 show BTX pull-down products of samples with and without recombinant GST-tagged truncated α1 nAChR or GST-tagged Lynx1. (D) GST pull-down assay of purified recombinant Lynx1-6xHis using GST-tagged α1, β1, δ, ε, or γ nAChR subunit ectodomains or GST alone (left lane). Western blot was performed with a 6XHis antibody (upper image) or GST antibody (lower image). n ≥ 3.

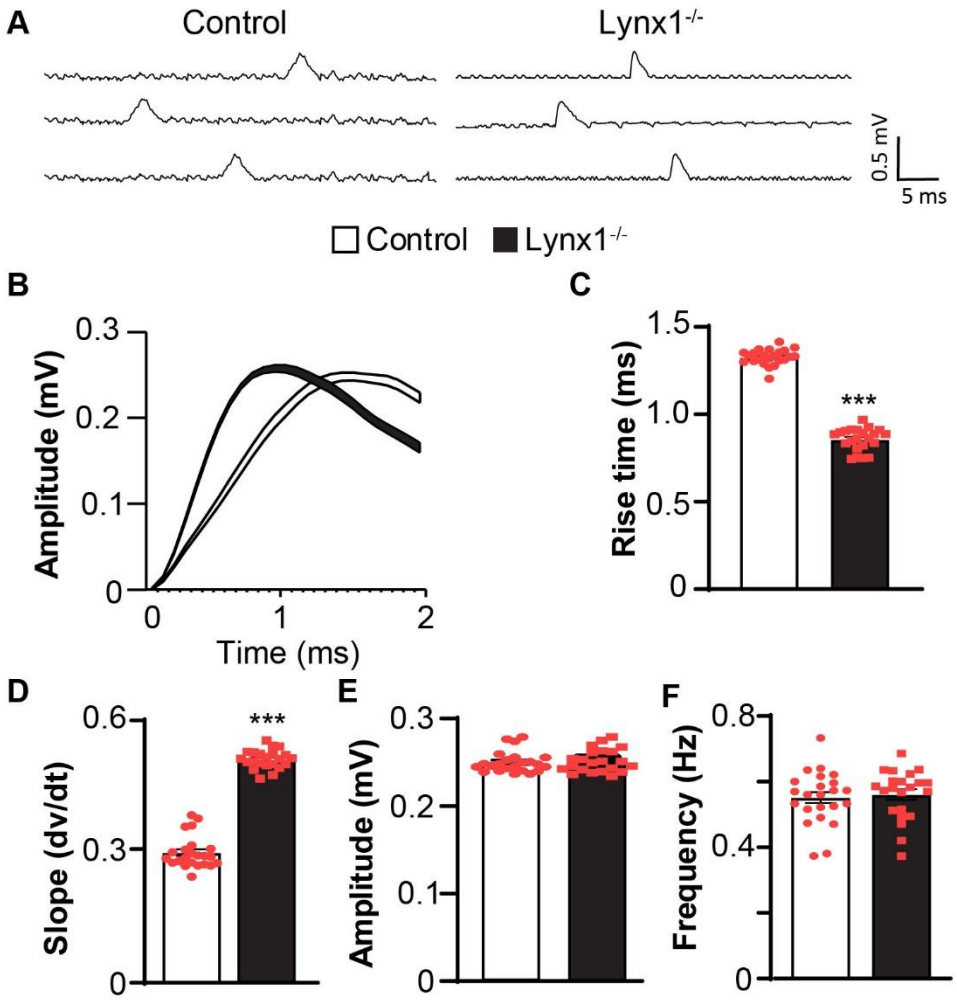

Figure 3. Lynx1 deletion increases nAChR sensitivity. (A) Example traces of spontaneous MEPP recordings from control and Lynx1$^{-/-}$ EDL. (B) Average MEPP amplitude of control and Lynx1$^{-/-}$ muscle, where the line width represents the SEM of 100 recordings. (C) Average rise time to peak amplitude of MEPPs represented in panel B. (D) Average slope of MEPPs to peak amplitude in panel B. (E) The mean amplitude of MEPPS in control and Lynx1$^{-/-}$ muscle. (F) The frequency of MEPPs control and Lynx1$^{-/-}$ muscle. Data represented as mean ± SEM. Control n ≥ 5, Lynx1-/- n ≥ 8. Statistical significance was determined with two-sided, unpaired Student's t-tests. ***p<0.001.

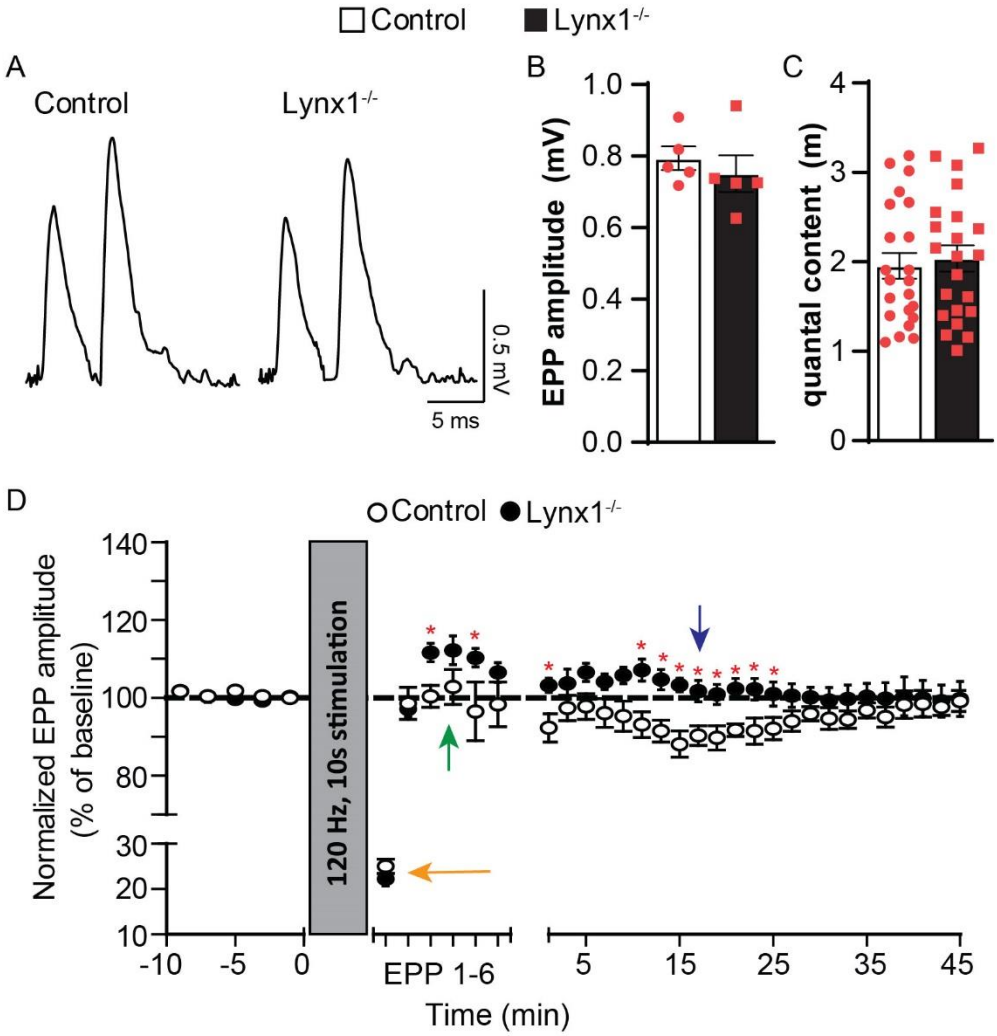

Figure 4. Lynx1 reduces synaptic plasticity. (A) Example recordings of EPPs elicited by paired-pulse stimulation (0.2 Hz, 10 ms interval) from control and Lynx1$^{-/-}$ EDL. (B) Average EPP amplitude (measured of the first EPP of the pair) and (C) the average quantal content following paired-pulse stimulation. (D) Amplitude of EPPs at baseline and following tetanic stimulation (120 Hz, 10s). The orange arrow denotes rapid depolarization following initial stimulation. The green arrow denotes post-tetanic potentiation in Lynx1$^{-/-}$ but not control muscle. The blue arrow denotes the absence of long-lasting depression in Lynx1$^{-/-}$ muscle. Data represented as means ± SEM. Control n ≥ 5, Lynx1$^{-/-}$ n ≥ 8. Statistical significance was determined with two-sided, unpaired Student's t-tests at each time point. *p<0.05.

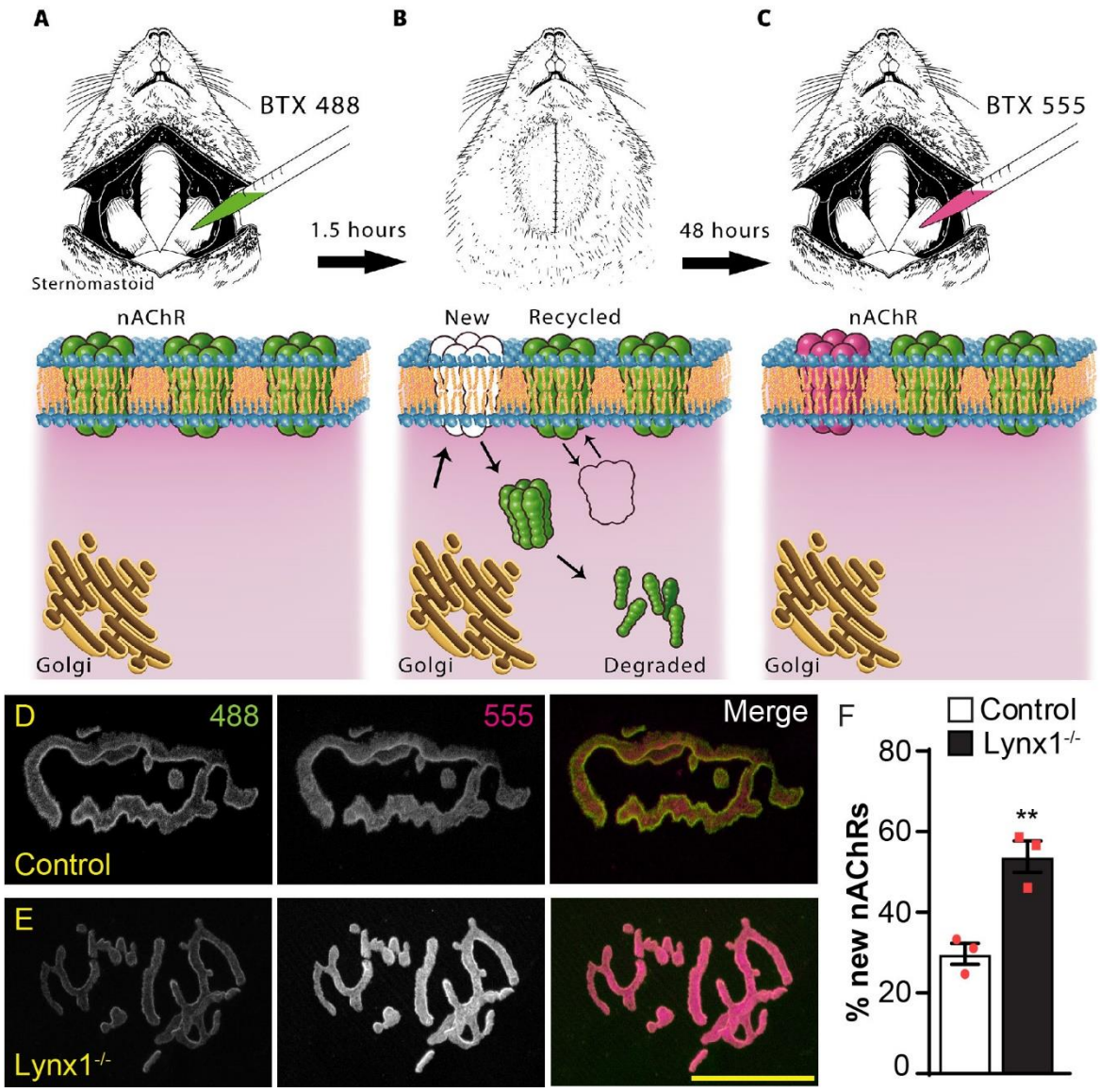

Figure 5. Loss of Lynx1 accelerates nAChR turnover in skeletal muscle. (A-C) Overview of nAChR labeling procedure to determine receptor turnover in the Sternomastoid muscles of 4 mo. mice. (A) The sternomastoid was surgically exposed and bathed in saturating levels of A488-BTX (green) for 1.5 hours. (B) The muscle was washed and the incision was sutured. (C) After 48 hours, the sternomastoid muscle was re-exposed and bathed in saturating levels of A555-BTX (magenta) for 1.5 hours. (D-E) Representative images of NMJs containing nAChRs labeled at the start of the experiment with A488-BTX (green) and newly inserted nAChRs labeled at the end of the experiment with A555-BTX (magenta) in the sternomastoid of control and Lynx1$^{-/-}$ mice. (F) A555-BTX pixel intensity as a percent of the sum of A488-BTX and A555-BTX pixel intensity at each NMJ was used to determine the percent of new nAChRs in control and Lynx1$^{-/-}$ mice. Data represented as mean ± SEM. Control n=4, Lynx1$^{-/-}$, n=4. At least 50 NMJs per animal were analyzed. Scale Bar = 30 µm. Statistical significance was determined with two-sided, unpaired Student's t-tests. **P<0.01

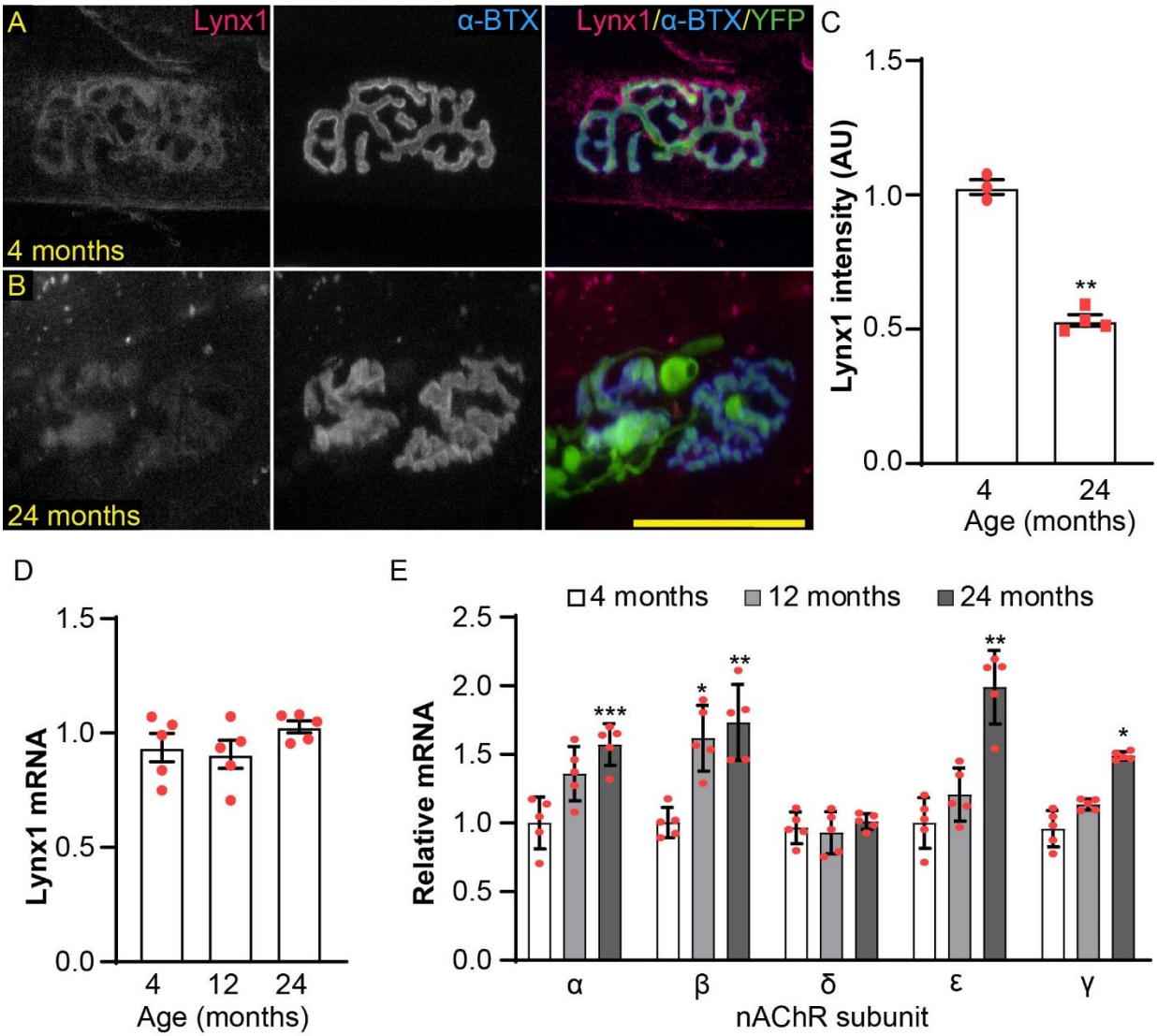

Figure 6. Endogenous Lynx1 expression in aging NMJs. (A-B) Representative images of immunohistochemistry with anti-Lynx1 (magenta), fBTX (blue), and YFP (green) in the EDL of 4 and 24 mo. control mice. (C) Pixel intensity analysis of fluorescently labeled Lynx1 revealed a loss of Lynx1 protein concentrated at the NMJ at 24 months of age. qPCR analysis of (D) Lynx1 mRNA levels and (E) nAChR subunits (α1, β1, δ, ε, and γ) in TA muscles from 4, 12, and 24 mo. control mice. Data represented as mean ± SEM. Expression is normalized to GAPDH using the $2^{-\Delta\Delta CT}$ method. n = 5. Scale Bar = 30 µm. Statistical significance was determined with two-sided, unpaired Student's t-tests. *P<0.05, **P<0.01, ***P<0.001 versus 4 mo. age group.

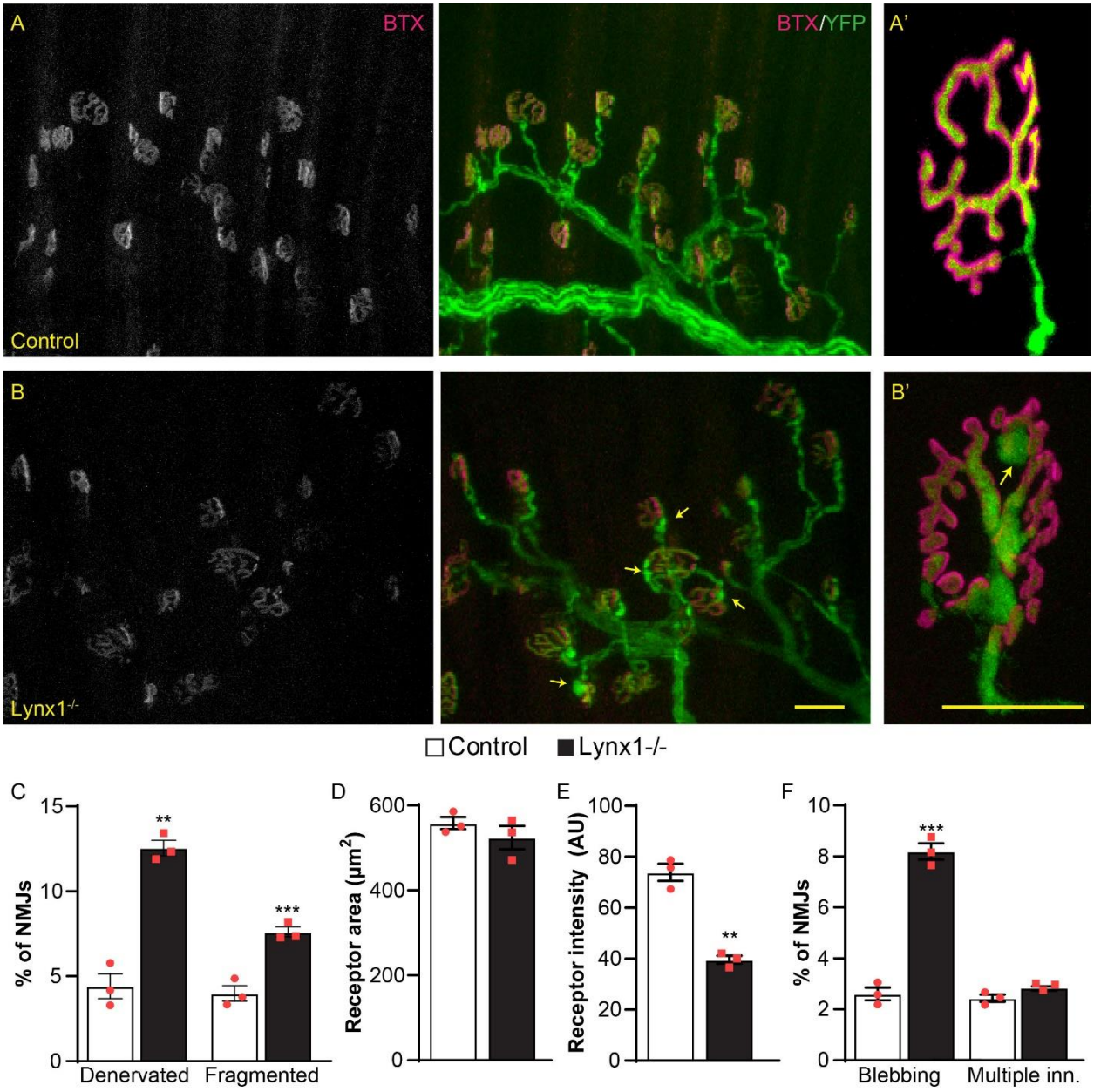

Figure 7. Lynx1 supports NMJ maintenance in young adult mice. (A-B) Representative images of NMJs in the EDL of 4 mo. control (A) and Lynx1$^{-/-}$ (B) mice. Motor axons were labeled with YFP (green) and nAChRs were labeled with fBTX (magenta). Arrows denote axon blebbing in Lynx1$^{-/-}$ EDL. (C) Percentage of denervated NMJs, either fully or partially, and NMJs with fragmented nAChR clusters containing 5 or more islands. (D) Average post-synaptic area of NMJs based on fBTX labeling of nAChRs. (E) Pixel intensity of fBTX-labeled nAChRs. (F) Percentage of NMJs with pre-synaptic abnormalities, including blebbing and innervation of a single NMJ by multiple axons. Data represented as mean ± SEM. Control n = 4, Lynx1$^{-/-}$ n = 5. At least 30 NMJs per animal were analyzed. Scale Bars = 30µm. Statistical significance was determined with two-sided, unpaired Student's t-tests. **P<0.01, ***P<0.001.

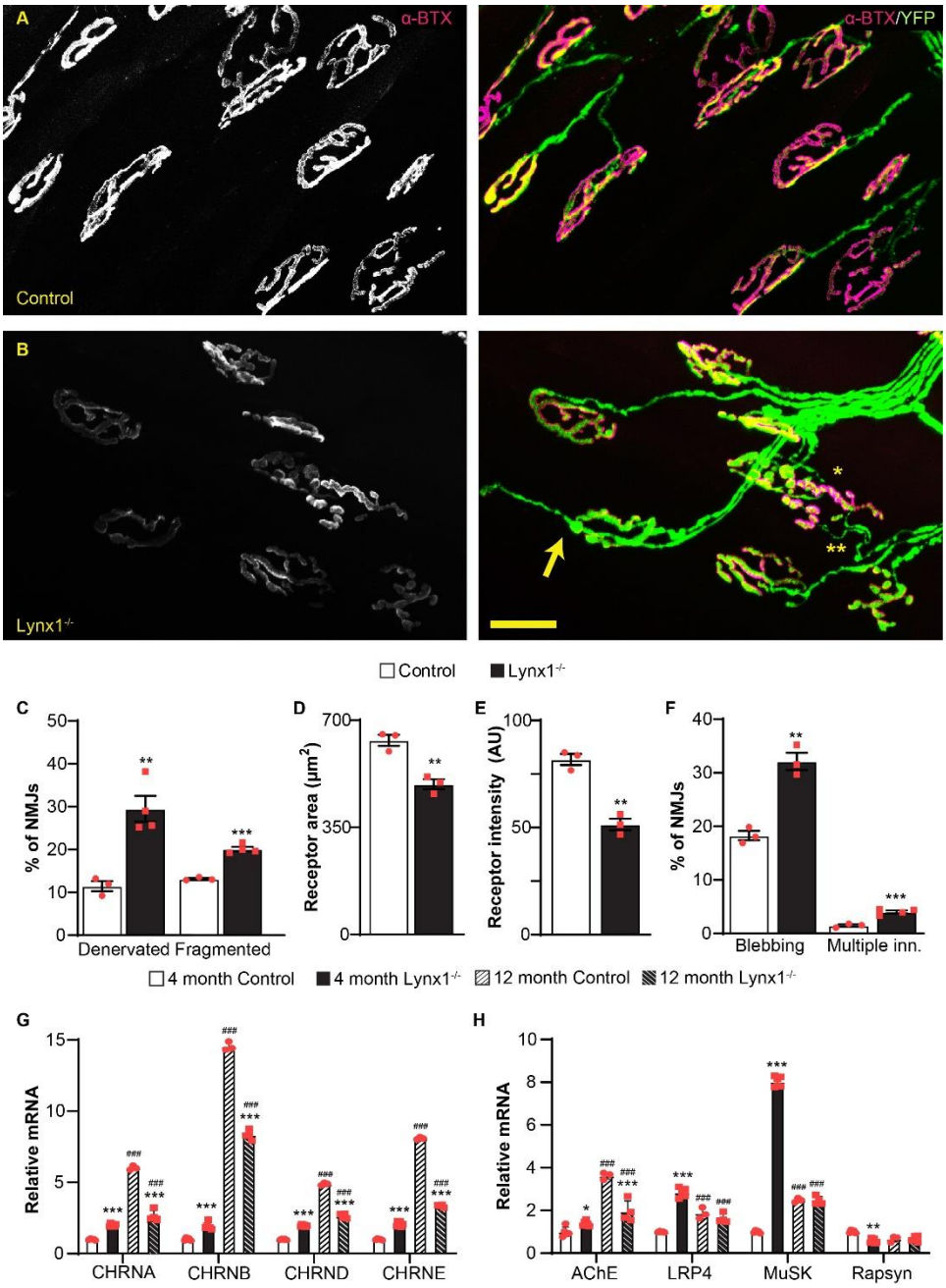

Figure 8. Lynx1 deletion accelerates age-related NMJ degeneration. (A-B) Representative images of NMJs in the EDL of 12 mo. control (A) and Lynx1$^{-/-}$ (B) mice. Motor axons were labeled with YFP (green) and nAChRs were labeled with fBTX (magenta). Arrows denote axon blebbing and asterisks denote NMJs that are both fragmented and denervated. (C) Percentage of denervated NMJs, either fully or partially, and NMJs with fragmented nAChR clusters containing 5 or more islands. (D) Average post-synaptic area of NMJs based on fBTX labeling of nAChRs. (E) Pixel intensity of fBTX-labeled nAChRs. (F) Percentage of NMJs with pre-synaptic abnormalities, including blebbing and innervation of a single NMJ by multiple axons. (G-H) qPCR analysis of α1, β1, δ, and ε nAChR subunits (G) and genes encoding synapse-enriched proteins (H) in TA muscles of 4 and 12 mo. control and Lynx1$^{-/-}$ mice (* indicates significant difference versus control, # indicates significant difference vs genotype-matched 4 mo. group). Data represented as mean ± SEM. Gene expression is relative to 4 mo. control and normalized to GAPDH using the $2^{-\Delta\Delta CT}$ method. n = 4. At least 30 NMJs per animal were analyzed. Scale Bar = 30 μm. For C-F, statistical significance was determined with two-sided, unpaired Student's t-tests. For G-H, statistical significance was determined with a 2-way ANOVA and Bonferroni post-hoc comparison of genotype and age effects. *P<0.05, **P<0.01, ***P<0.001.

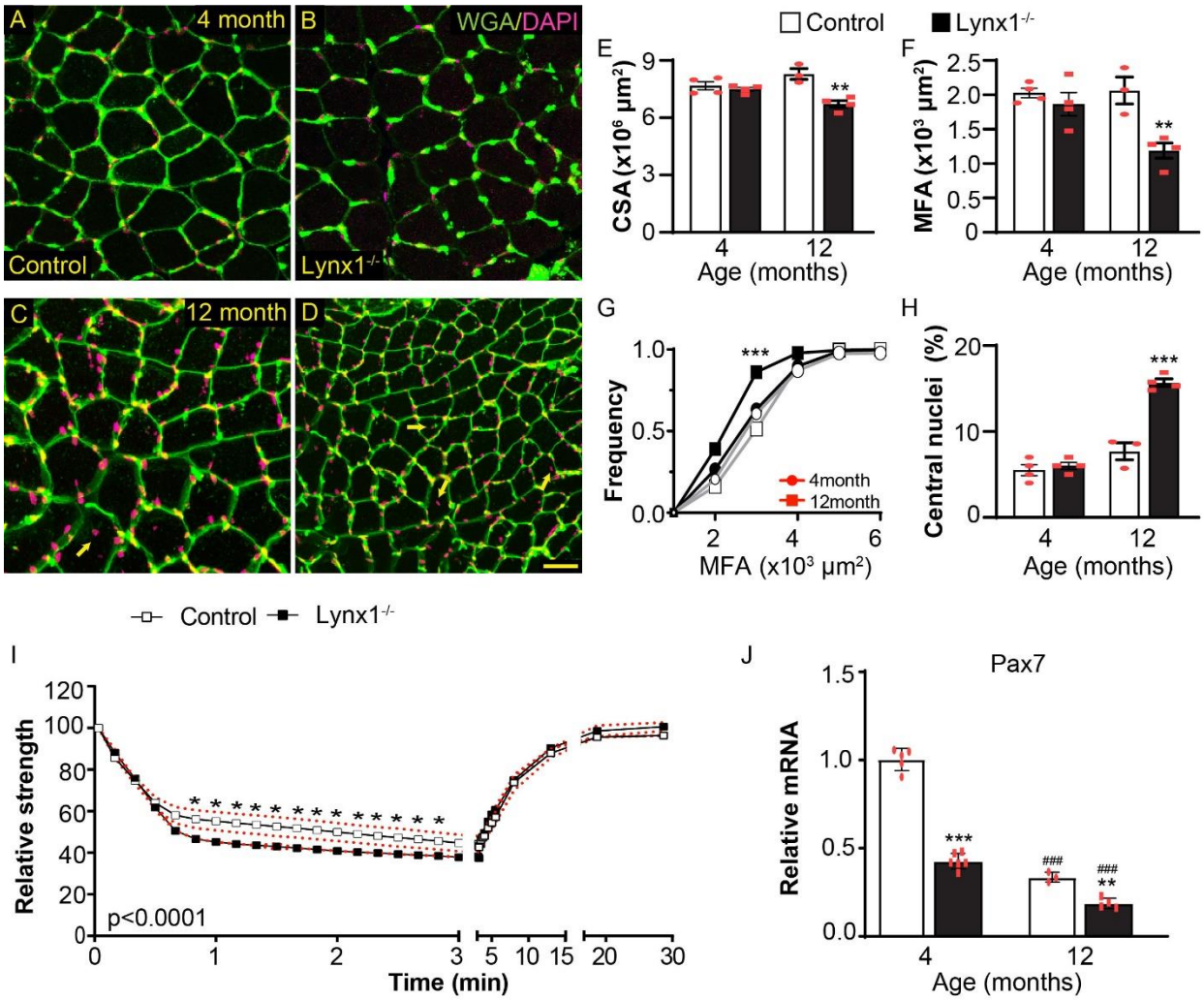

Figure 9. Lynx1 deletion causes muscle atrophy in middle-aged mice. (A-D) Representative images of TA cross sections from 4 and 12 mo. control and Lynx1$^{-/-}$ mice in which muscle fibers are identified with WGA (green) and nuclei are labeled with DAPI (magenta). Arrows denote muscle fibers with a central nucleus. (E) Average TA CSA. (F) Average muscle fiber CSA. (G) Cumulative frequency analysis of MFAs. (H) Quantification of the percentage of muscle fibers with a centrally located nucleus. (I) Neuromuscular fatigue represented as relative strength, as a percent of baseline, following super-imposed muscle stimulations after fatigue protocol in 4 mo. control and Lynx1$^{-/-}$ EDL (red dotted line represents SEM). (J) qPCR analysis of Pax7, a marker of muscle satellite cells, mRNA levels in 4 and 12 mo. control and Lynx1$^{-/-}$ TA. Data represented as mean ± SEM. Gene expression is relative to 4 mo. control and normalized to GAPDH using the $2^{-\Delta\Delta CT}$ method. Control, n ≥ 3; Lynx1$^{-/-}$, n ≥ 4; for all panels except I, where control, n ≥ 5; Lynx1$^{-/-}$, n ≥ 8. At least 100 muscle fibers per animal were analyzed. Statistical significance was determined using 2-way ANOVA and Bonferroni post-hoc comparison of genotype and age effects for all panels except G (Kolmogorov–Smirnov test) and I (two-sided, unpaired Student's t-test). Scale Bar = 30µm. *P<0.05, **P<0.01, and ***P<0.001 versus control. ### P<0.001 versus genotype-matched 4 mo. group.

Table 1. qPCR primers sequences.

Gene	Forward Primer (5'-3')	Reverse Primer (5'-3')
AChE	CTACACCACGGAGGAGAGGA	CTGGTTCTTCCAGTGCACCA
Atrogin-1	GCAGCAGCTGAATAGCATCCA	GGTGATCGTGAGGCCTTTGAA
CHRNα1	CTTCAAAGAGCTTTGCCACC	CCATGGAGCTCTCGACTGTT
CHRNβ1	AGGTCTCAGGCACTTTGTCG	TTCTACCTCCCACCAGATGC
CHRNγ	GCTCAGCTGCAAGTTGATCTC	CCTCCTGCTCCATCTCTGTC
CHRNδ	CCGATGCACTATCTCCCACT	CTTAGCCTGAAGCAGGAGGA
CHRNε	GCTGTGTGGATGCTGTGAAC	GCTGCCCAAAAACAGACATT
FGFBP1	CTGCATTCCCCAGTACACCT	GCCAGGAGAAGGAAGGAGAG
FOXO-1	GAGTTAGTGAGCAGGCTACATTT	TTGGACTGCTCCTCAGTTCC
GAPDH	CCCACTCTTCCACCTTCGATG	GTCCACCACCCTGTTGCTGTAG
GDNF	GCCACCATTAAAAGACTGAAAAGG	GCCTGCCGATTCCTCTCTCT
LRP4	GGCAAAAAGCAGGAACTTGT	TCTACCCAGTGGCCAGAACT
Lynx1	ACCACTCGAACTTACTTCACC	ATCGTACACGGTCTCAAAGC
MTND1	GTTGGTCCATACGGCATTTT	TGGGTGTGGTATTGGTAGGG
mTOR	TTCAATCCATAGCCCCGTCT	CAAAGAGCTGCATCACTCGT
MuSK	CCGATGTGTCTGCTCTTTGA	ACAGGACAGTGGTGGAGGAC
Myogenin	ACCAGGAGCCCCACTTCTAT	GTCCCCAGTCCCTTTTCTTC
Pax7	GCGAGAAGAAAGCCAAACAC	GTCGGGTTCTGATTCCACAT
PGC1α	CCCTGCCATTGTTAAGACC	TGCTGCTGTTCCTGTTTTC
PKM1	GCTGTTTGAAGAGCTTGTGC	TTATAAGAGGCCTCCACGCT
PKM2	TCGCATGCAGCACCTGATT	CCTCGAATAGCTGCAAGTGGTA

PPARγ	TGTGGGGATAAAGCATCAGGC	CCGGCAGTTAAGATCACACCTAT
Rapsyn	GTGCCATGGAGTGTTGTGAG	CGGTTTCCGATCTCAGTCAT
SirT1	AGAACCACCAAAGCGGAAA	TCCCACAGGAGACAGAAACC
TGFβ	CCCGAAGCGGACTACTATGC	CATAGATGGCGTTGTTGCGG

Supplementary Materials

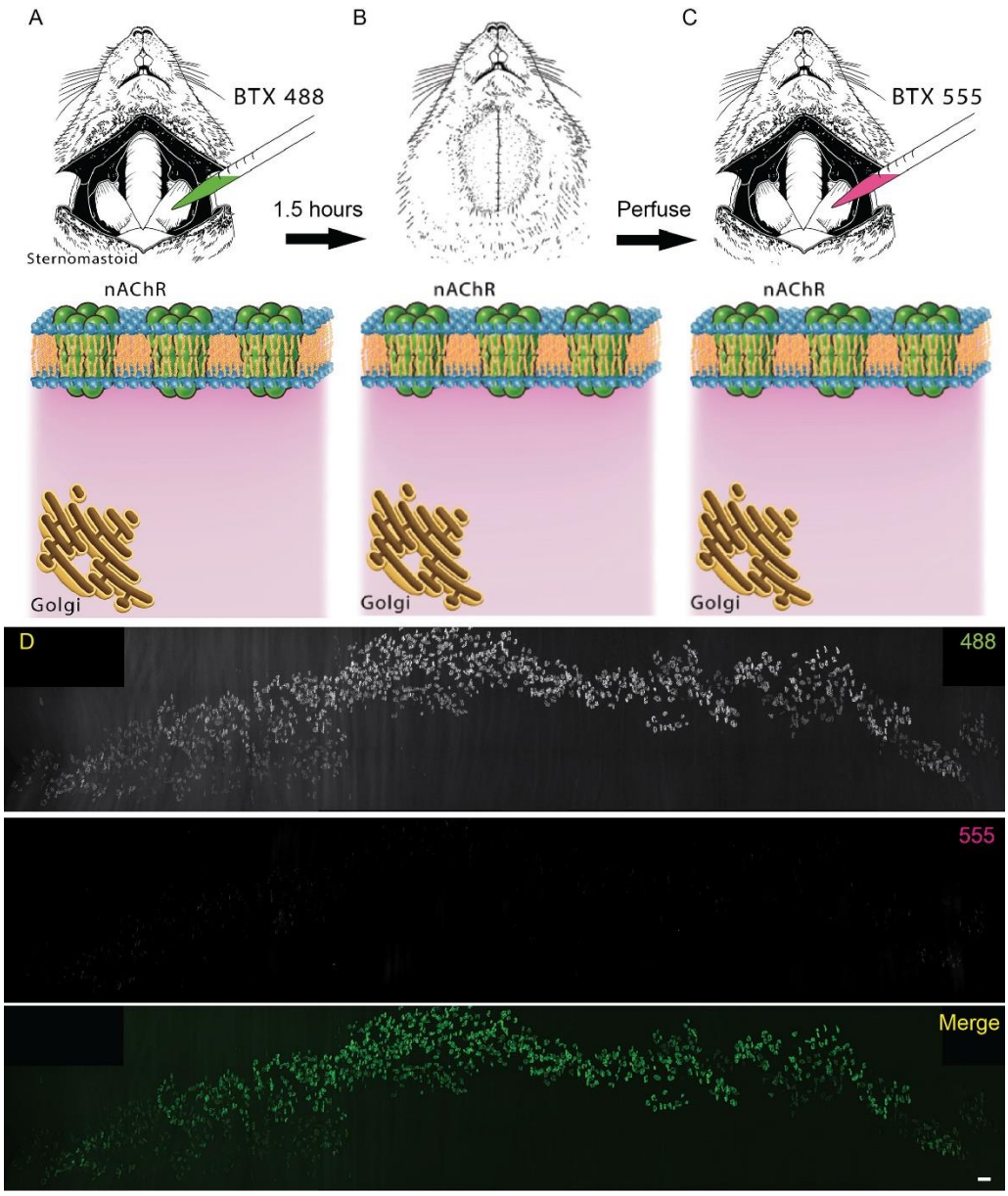

Supplementary Figure 1. nAChR saturation following fBTX exposure. (A-C) Overview of nAChR labeling procedure to determine receptor saturation. (A) Sternomastoid muscles of 4 mo. mice were surgically exposed and bathed in saturating levels of A488-BTX (green) for 1.5 hours. (B) The muscles were washed and immediately fixed with PFA. (C) Sternomastoid muscles were subsequently bathed in saturating levels of A555-BTX (magenta) for 1.5 hours and then imaged. (D) Representative images of NMJs within the sternomastoid showing a large number of A488-BTX labeled NMJs (green) with little A555-BTX labeled NMJs (magenta) demonstrating that A488-BTX saturated nAChRs within the muscle. Scale bar = 100 µm.

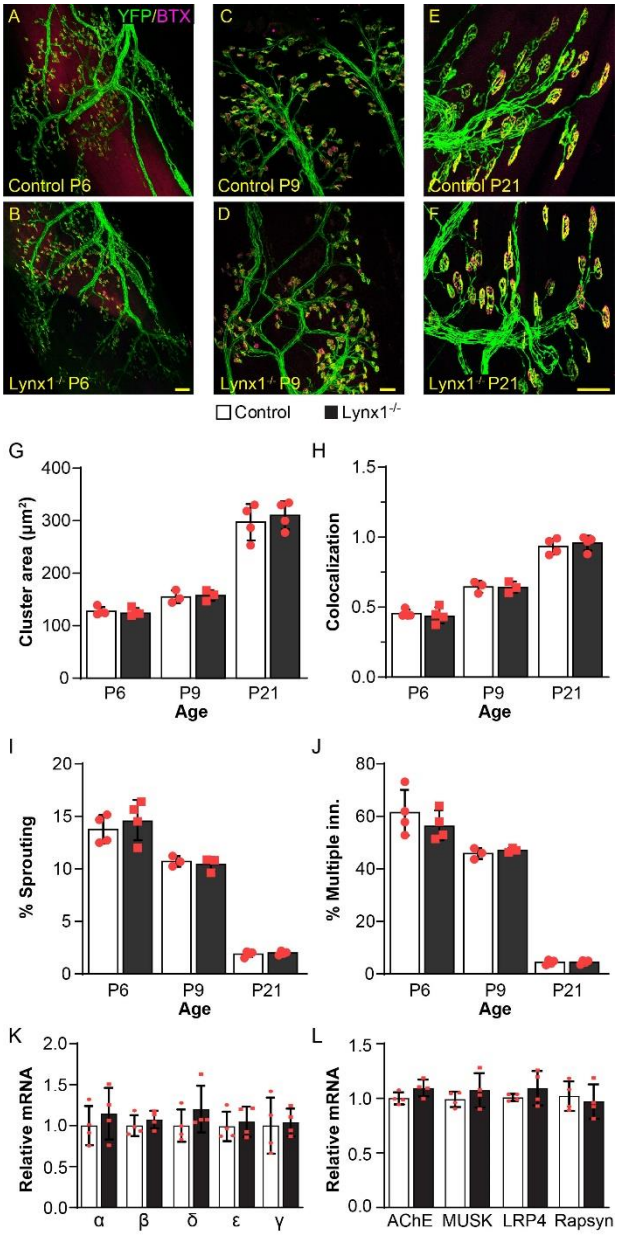

Supplementary Figure 2. Loss of Lynx1 has no discernable impact on NMJ development. (A-F) Representative images of NMJs in the EDL muscles of P6 (A,B), P9 (C,D), and P21 (E,F) control and Lynx1$^{-/-}$ mice. Motor axons were labeled with YFP (green) and nAChRs were labeled with fBTX (magenta). (G-L) Morphological analysis of NMJs, including (G) NMJ area, as determined by the area of nAChR clusters, (H) degree of NMJ innervation, as determined by colocalization of YFP and fBTX pixels, (I) percentage of NMJs with axonal sprouts, (J) percentage of NMJs that were innervated by more than one axon. (K-L) qPCR analysis of mRNA levels of genes encoding proteins that are enriched at the NMJ, including (K) α1, β1, δ, ε, and γ nAChR subunits and (L) AChE, MuSK, LRP4, and Rapsyn. Data represented as mean ± SEM. Expression is normalized to GAPDH using the $2^{-\Delta\Delta CT}$ method. Control, n ≥ 3; Lynx1$^{-/-}$, n ≥ 3. At least 50 NMJs per animal were analyzed. Scale bar = 20 µm.

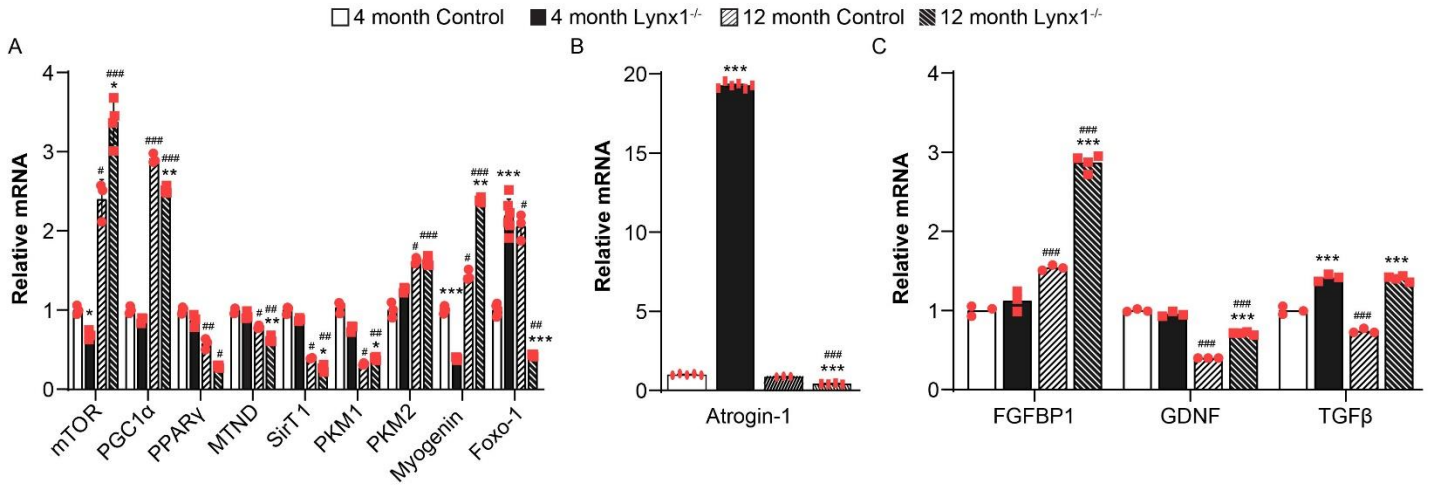

Supplementary Figure 3. Expression analysis of genes associated with skeletal muscle health. qPCR analysis of gene expression in the TA of 4 mo. and 12 mo. control and Lynx1$^{-/-}$ mice. (A) Genes associated with metabolism and muscle atrophy. (B) Atrogin-1. (C) Secreted proteins and growth factors. Data represented as mean ± SEM. Expression is normalized to GAPDH using the $2^{-\Delta\Delta CT}$ method. Control, n ≥ 3; Lynx1$^{-/-}$, n = 4. Statistical significance was determined using 2-way ANOVA and Bonferroni post-hoc comparison of genotype and age effects. *P<0.05, **P<0.01, ***P<0.001.